Chapter 2

Global Chemical Model of the Troposphere

2.1 Introduction

As discussed in the previous chapter, tropospheric ozone and related chemistry have significant roles in the climate system and atmospheric environment. With limited observations available for tropospheric chemistry involving ozone distribution, numerical models are needed to investigate tropospheric ozone chemistry and to assess its impact on global climate (e.g., global radiative forcing from tropospheric ozone). There have been various global modeling studies of tropospheric ozone, chemistry, and transport up to the present [*Levy et al.*, 1985; *Crutzen and Zimmermann*, 1991; *Roelofs and Lelieveld*, 1995; *Müller and Brasseur*, 1995; *Roelofs et al.*, 1997; *Berntsen and Isaksen*, 1997a; *Wang et al.*, 1998a, b; *Brasseur et al.*, 1998; *Hauglustaine et al.*, 1998; *Lawrence et al.*, 1999; *Horowitz et al.*, 2002]. Models in those studies generally include photochemical reactions in the troposphere to consider ozone formation and destruction. The photochemical chain reaction which produces ozone is initiated and maintained by reactive radicals as illustrated in Figure 2.1. While volatile organic compounds (VOCs) act as "fuel" in the ozone formation process, NO_x ($= NO + NO_2$), most important species, partially function as a catalysis "engine" in the formation process (NO also plays a key role in the regeneration of the reactive radicals and the further progress of the reactions). In the process, other important products such as peroxy acetyl nitrate, nitric acid, aldehydes, organic acids, particulates and many short-lived radical species are formed from the VOCs degradation. The significance of VOCs in the ozone formation process increases in the polluted (NO_x rich) atmospheres as in urban sites [*Chameides et al.*, 1992; *Konovalov*, 2002]. Also, VOCs, reacting with OH rapidly, have great impacts on the global OH radical field, oxidizing capacity of the atmosphere. However, several of the above global models ignore higher VOCs (non-methane hydrocarbons, NMHCs) and employ a simple NO_x-CH_4-CO chemistry [e.g., *Roelofs and Lelieveld*, 1995; *Lawrence et al.*, 1999], because of heavy demands on computer time by NMHCs chemistry. The previous studies of *Müller and Brasseur* [1995], *Wang et al.* [1998a, b], *Brasseur et al.* [1998], *Hauglustaine et al.* [1998], and *Horowitz et al.* [2002] have simulated global tropospheric chemistry including NMHCs. The simulations of *Wang et al.* [1998c], *Horowitz et al.* [1998], and *Roelofs and Lelieveld* [2000] reported the influence of NMHCs (particularly of iso-

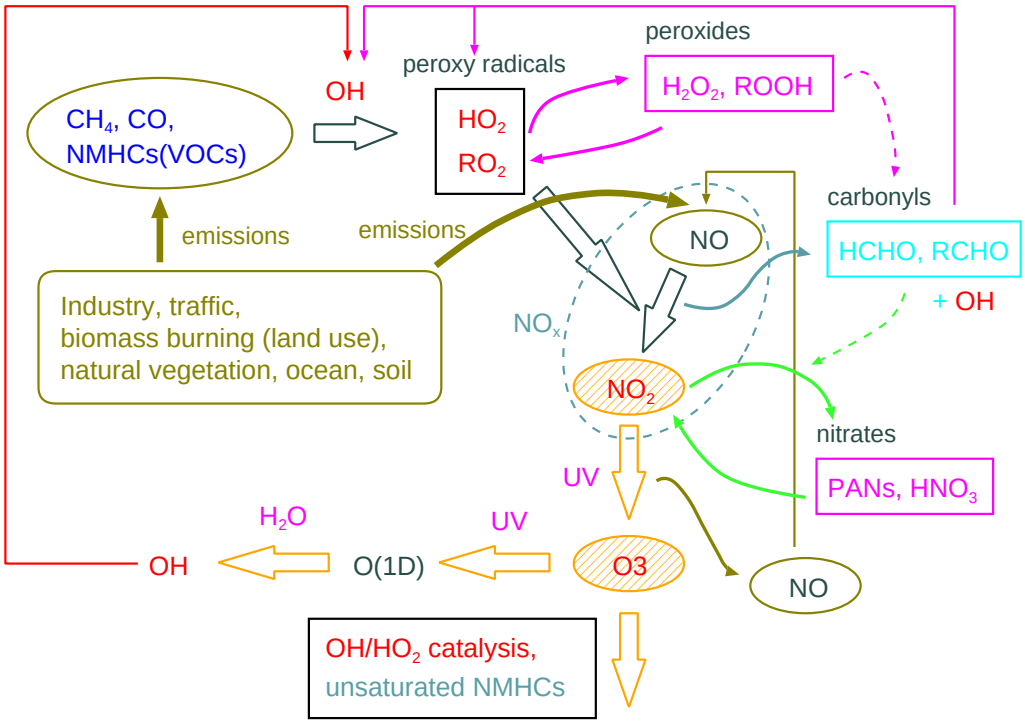

Figure 2.1. The fundamental flow of tropospheric chemistry producing ozone from NO_x and hydrocarbons. Also shown is formation of reservoir species like peroxides and nitrates.

prene) on ozone formation and the global OH field.

Many of the global chemical models developed so far use meteorological variables such as wind and temperature prescribed "off-line" without considering the feedback from tropospheric ozone forcing [*Müller and Brasseur*, 1995; *Berntsen and Isaksen*, 1997a; *Horowitz et al.*, 1998; *Haywood et al.*, 1998; *Wang et al.*, 1998a; *Brasseur et al.*, 1998]. This kinds of models ignore the short-term and synoptic-scale correlations between tropospheric ozone and meteorological variables such as clouds and temperature [*Pickering et al.*, 1992; *Sillman and Samson*, 1995], and may not be suitable for accurate simulation of the future climate system. On the contrary, several model studies consider "on-line" simulation of tropospheric ozone and meteorology, incorporating chemistry into general circulation models (GCMs) [e.g., *Roelofs and Lelieveld*, 1995, 2000; *Mickley et al.*, 1999]. While such models are useful to investigate interactions between tropospheric chemistry and climate, they are computationally heavy in general and may have limitations in spatial resolution compared to "off-line" models.

In this study, a global chemical model for the troposphere has been developed. The model, named CHemical AGCM for Study of atmospheric Environment and Radiative forcing (CHASER), has been developed in the framework of the Center for Climate System Research (CCSR), University of Tokyo/National Institute for Environmental Studies (NIES) atmospheric GCM (AGCM). This model, CHASER, is aimed to study tropospheric ozone and related chemistry, and their impacts on climate. The model includes a detailed simulation of tropospheric chemistry including

NMHCs. The chemistry component is coupled with the CCSR/NIES AGCM to allow the interactions between climate and tropospheric chemistry (i.e., ozone and CH_4 distributions) in the model. As mentioned in the previous chapter, tropospheric ozone chemistry is much responsible for formation of sulfate which has significant direct/indirect climate effects (Figure 1.1). As the sulfate formation process is important in the climate system as well as ozone, and in turn has some impacts on tropospheric chemistry especially on hydrogen peroxide (H_2O_2), it was opted to be simulated on-line in the present version of CHASER. Although sulfate simulation is implemented and is reflected on the calculation of heterogeneous reactions in the model, note that it is not linked to the radiative transfer code in the AGCM at this stage.

The following sections present description and evaluation of the CHASER model which is based on the CCSR/NIES AGCM. The CCSR/NIES AGCM has been also used for an on-line global simulation of stratospheric chemistry and dynamics [*Takigawa et al.*, 1999], and for a global simulation of the aerosol distribution and optical thickness of various origins [*Takemura et al.*, 2000, 2001]. The principal objective of CHASER is to investigate the global distributions and budgets of ozone and related tracers, and the radiative forcing from tropospheric ozone. Additionally, CHASER can be used to assess the global impact of changes in the atmospheric composition on climate. Principal description and evaluation of the CHASER model (the previous version) are presented in *Sudo et al.* [2002a, b]. CHASER has been employed in a simulation study of tropospheric ozone changes during the 1997-1998 El Niño event [*Sudo and Takahashi*, 2001] (see chapter 4).

A detailed description of the present version of CHASER is given in section 2.2 which includes descriptions of chemistry, emissions, deposition processes. In section 2.3, model results are evaluated in detail with a number of observations. Conclusions from this model development are in section 2.4. In the end of this chapter, evaluation of transport and deposition processes and description of aqueous-phase reactions implemented in the model are given (Appendix 2A, B, respectively).

2.2 Model description

As mentioned above, the CHASER model is based on the CCSR/NIES atmospheric general circulation model (AGCM). The present version of CHASER uses the CCSR/NIES AGCM, version 5.6. Basic features of the CCSR/NIES AGCM have been described by *Numaguti* [1993]. The newly implemented physical processes were presented by *Numaguti et al.* [1995]. This AGCM adopts a radiation scheme based on the k-distribution and the two-stream discrete ordinate method [*Nakajima and Tanaka*, 1986]. A detailed description of the radiation scheme adopted in the AGCM is given by *Nakajima et al.* [1995]. The prognostic Arakawa-Schubert scheme is employed to simulate cumulus (moist) convection [cf. *Numaguti et al.*, 1995]. *Emori et al.* [2001] evaluates the cumulus convection scheme in a simulation of precipitation over East Asia. (see also the description by *Numaguti* [1999] for further details of the hydrological processes in the model). The level 2 scheme of turbulence closure by *Mellor and Yamada* [1974] is used for the estimation of the vertical diffusion

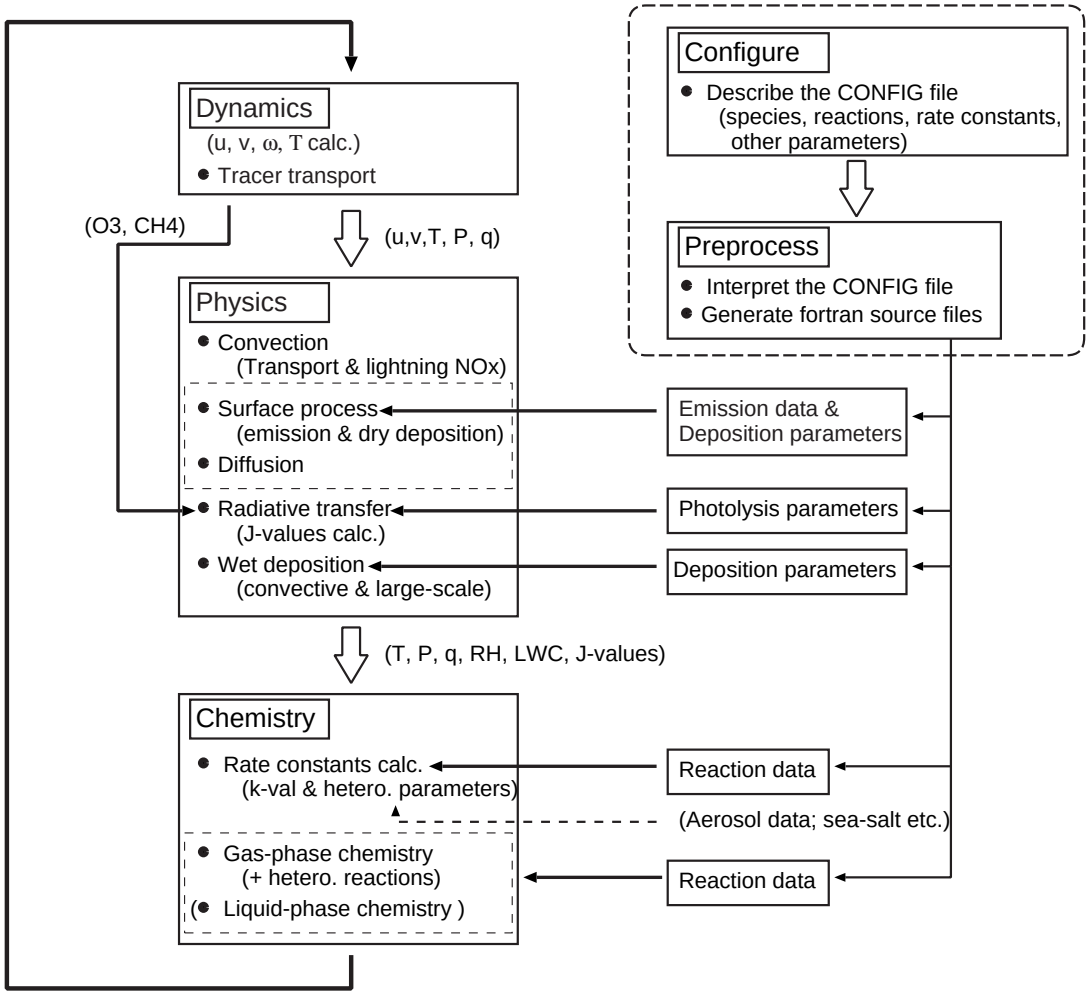

Figure 2.2. The flow of calculation in the CHASER model. Dynamics, physics, chemistry processes are evaluated at each time step in the CCSR/NIES AGCM. Configurations of the chemical scheme such as a choice of species, reactions and reaction rates are automatically processed by the preprocessor to set up the model through input files

coefficient. The orographic gravity wave momentum deposition in the AGCM is parameterized following *McFarlane* [1987]. The AGCM generally reproduces the climatology of meteorological fields. In climatological simulations, CHASER uses climatological data of sea surface temperature (SST) as an input to the AGCM. In simulations of a specific time period, analyzed data of wind velocities, temperature, and specific humidity from the European Center for Medium-Range Weather Forecasts (ECMWF) are used as a constraint in addition to SST data of a corresponding year, because it may be difficult to validate just climatological output from the model with observations in a certain period.

In CHASER, dynamical and physical processes such as tracer transport, vertical diffusion, surface emissions, and deposition are simulated in the flow of the AGCM calculation (Figure 2.2). The chemistry component of CHASER calculates chemical transformations (gas and liquid phase

chemistry and heterogeneous reactions) using variables of the AGCM (temperature, pressure, humidity, etc.). In the radiation component, radiative transfer and photolysis rates are calculated by using the concentrations of chemical species calculated in the chemistry component. The dynamical and physical components of CHASER are evaluated with a time step of 20 or 30 min. Time step for chemical reactions in this study is opted to be 10 min. In this study, the model adopts a horizontal spectral resolution of T42 (approximately, 2.8° longitude $\times$ 2.8° latitude) with 32 layers in the vertical from the surface up to about 3 hPa (about 40 km) altitude. CHASER uses the σ coordinate system in the vertical. The 32 layers are centered approximately at 995, 980, 950, 900, 830, 745, 657, 576, 501, 436, 380, 331, 288, 250, 218, 190, 165, 144, 125, 109, 95, 82, 72, 62, 54, 47, 40, 34, 27, 19, 11, and 3 hPa, resulting in a vertical resolution of 1 km in the free troposphere and much of the lower stratosphere for an accurate representation of vertical transport such as the stratosphere-troposphere exchange (STE).

The present version of CHASER calculates the concentrations of 53 chemical species from the surface up to about 20 km altitude. The concentrations of O_3, NO_x, N_2O_5, and HNO_3 in the stratosphere (above 20 km altitude) are prescribed using monthly averaged output data from a three-dimensional stratospheric chemical model [*Takigawa et al.*, 1999]. For the O_3 distribution ($>$ 20 km), the data of *Takigawa et al.* [1999] were scaled by using zonal mean satellite data from the Halogen Occultation Experiment project (HALOE) [*Russel et al.*, 1993; *Randel*, 1998], since the latest version of the stratospheric chemical model [*Takigawa et al.*, 1999] tends to slightly overestimate the O_3 concentrations in the tropical lower stratosphere. The concentrations in the stratosphere ($>$ 20km) in the model are nudged to those data with a relaxation time of one day at each time step.

In CHASER, advective transport is simulated by a 4th order flux-form advection scheme of the monotonic van Leer [*van Leer*, 1977], except for the vicinity of the poles. For a simulation of advection around the poles, the flux-form semi-Lagrangian scheme of *Lin and Rood* [1996] is used. Vertical transport associated with moist convection (updrafts and downdrafts) is simulated in the framework of the cumulus convection scheme (the prognostic Arakawa-Schubert scheme) in the AGCM. In the boundary layer, equations of vertical diffusion and surface emission and deposition fluxes are solved implicitly. The adopted transport scheme is evaluated in Appendix 2A (page 102) together with evaluation of the deposition scheme.

Information about the CHASER model can also be obtained via the CHASER web site (http://atmos.ccsr.u-tokyo.ac.jp/~kengo/chaser).

2.2.1 Chemistry

The chemistry component of CHASER includes 37 tracers (transported) and 17 non-tracers (radical species and members of family tracers). Table 2.1 shows chemical species considered in CHASER. Ozone and nitrogen oxides ($NO + NO_2 + NO_3$) are transported as families (O_x and NO_x respectively). The concentrations of nitrogen (N_2), oxygen (O_2), water vapor (H_2O), and

Table 2.1. Chemical Species Considered in CHASER

No.	Name	Family [a]	Description
Tracers			
01	O_x	$O_3 + O + O(^1D)$	O_x family (ozone and atmoic oxygen)
02	NO_x	$NO + NO_2 + NO_3$	NO_x family
03	N_2O_5	single	nitrogen pentoxide
04	HNO_3	single	nitric acid
05	HNO_4	single	peroxynitric acid
06	H_2O_2	single	hydrogen peroxide
07	CO	single	carbon monoxide
08	C_2H_6	single	ethane
09	C_3H_8	single	propane
10	C_2H_4	single	ethene
11	C_3H_6	single	propene
12	ONMV	single	other NMVOCs [b]
13	C_5H_8	single	isoprene
14	$C_{10}H_{16}$	single	terpenes
15	CH_3COCH_3	single	acetone
16	CH_2O	single	formaldehyde
17	CH_3CHO	single	acetaldehyde
18	NALD	single	nitrooxy acetaldehyde
19	MGLY	single	methylglyoxal and other C_3 aldehydes
20	HACET	single	hydroxyacetone and C_3 ketones
21	MACR	single	methacrolein, methylvinylketone and C_4 carbonyls
22	PAN	single	peroxyacetyl nitrate
23	MPAN	single	higher peroxyacetyl nitrates
24	ISON	single	isoprene nitrates
25	CH_3OOH	single	methyl hydro-peroxide
26	C_2H_5OOH	single	ethyl hydro-peroxide
27	C_3H_7OOH	single	propyl hydro-peroxide
28	HOROOH	single	peroxides from C_2H_4 and C_3H_6
29	ISOOH	single	hydro-peroxides from $ISO_2 + HO_2$
30	CH_3COOOH	single	paracetic acid
31	MACROOH	single	hydro-peroxides from $MACRO_2 + HO_2$
32	O_x(S)	O_3(S) + $O(^1D)$(S)	O_x family from the stratosphere
33	SO_2	single	sulfur dioxide
34	DMS	single	dimethyl sulfide
35	SO_4	single	sulfate (non sea-salt)
36	^{222}Rn	single	radon(222)
37	^{210}Pb	single	lead(210)
Non-Tracers [c]			
01	OH		hydroxyl radical
02	HO2		hydroperoxyl radical
03	CH_3O2		methyl peroxy radical
04	C_2H_5O2		ethyl peroxy radical
05	C_3H_7O2		propyl peroxy radical
06	CH_3COO_2		peroxy acetyl radical
07	$CH_3COCH_2O_2$		acetylmethyl peroxy radical
08	$HOC_2H_4O_2$		hydroxy ethyl peroxy radical
09	$HOC_3H_6O_2$		hydroxy propyl peroxy radical
10	ISO_2		peroxy radicals from $C_5H_8 + OH$

Table 2.1. (continued)

No.	Name	Family [a]	Description
11	$MACRO_2$		peroxy radicals from MACR + OH
12	$CH_3SCH_2O_2$		dimethyl sulfide peroxy radical

[a]For transport
[b]Non Methane Volatile Organic Compounds
[c]Not including member species of family tracers

hydrogen (H_2) are determined from the AGCM calculation. In this study, CH_4 is not considered as a tracer because of uncertainty in the natural emission amount of CH_4 and its long chemical lifetime (8-11 years). In the model, CH_4 concentration is assumed to be 1.77 ppmv and 1.68 ppmv in the northern and the southern hemisphere, respectively. N_2O concentration in the model is also fixed to 0.3 ppmv uniformally in the global.

The present version of CHASER includes 26 photolytic reactions and 111 chemical reactions including heterogenous and aqueous-phase reactions (Table 2.2 and Table 2.3). It considers NMHCs oxidation as well as the O_x-HO_x-NO_x-CH_4-CO chemical system. Oxidations of ethane (C_2H_6), propane (C_3H_8), ethene (C_2H_4), propene (C_3H_6), isoprene (C_5H_8), and terpenes ($C_{10}H_{16}$, etc.) are included explicitly. Degradation of other NMHCs is represented by the oxidation of a lumped species named other non-methane volatile organic compounds (ONMV) as in the IMAGES model [*Müller and Brasseur*, 1995] and the MOZART model [*Brasseur et al.*, 1998]. The model adopted a condensed isoprene oxidation scheme of *Pöschl et al.* [2000] which is based on the Master Chemical Mechanism (MCM, Version 2.0) [*Jenkin et al.*, 1997]. Terpenes oxidation is largely based on *Brasseur et al.* [1998] (the MOZART model). Acetone is believed to be an important source of HO_x in the upper troposphere and affect the background PAN formation in spite of its low photochemical activity. Acetone chemistry and propane oxidation are, therefore, included in this study, based on the MCM, Version 2.0.

Dentener and Crutzen [1993] suggested that heterogeneous hydrosis of N_2O_5 on aqueous-phase aerosols can reduce NO_x levels and hence ozone production in polluted areas. In addition, several studies have shown the possibility that heterogeneous reactions of HO_2 and some peroxy radicals (RO_2) from unsaturated hydrocarbons like isoprene may occur on aqueous-phase aerosols [*Jaeglé et al.*, 1999; *Jacob*, 2000]. *Meilinger et al.* [2001] have also suggested an importance of heterogeneous reactions on liquid and ice (cirrus) clouds for the ozone and HO_x budgets in the tropopause region. In this study, the heterogeneous reaction of "$N_2O_5 \rightarrow 2\ HNO_3$" is included with an uptake coefficient γ of 0.1 on aqueous-phase aerosols and 0.01 on ice particles [*Sander et al.*, 2000]. Reactions of HO_2 and RO_2 on aerosols are tentatively included in this study as listed in Table 2.3, with γ values based on *Jacob* [2000]. The heterogeneous loss rate β for the species i

Table 2.2. Photolytic Reactions Included in CHASER

No.	Reaction	Ref.
J1)	$O_3 + h\nu \rightarrow O(^1D) + O_2$	1,2
J2)	$O_3 + h\nu \rightarrow O + O_2$	1,2
J3)	$H_2O_2 + h\nu \rightarrow 2\ OH$	1
J4)	$NO_2 + h\nu \rightarrow NO + O$	1
J5)	$NO_3 + h\nu \rightarrow 0.1\ NO + 0.9\ NO_2 + 0.9\ O_3$	1
J6)	$N_2O_5 + h\nu \rightarrow NO_2 + NO_3$	1
J7)	$HNO_3 + h\nu \rightarrow NO_2 + OH$	1
J8)	$HNO_4 + h\nu \rightarrow NO_2 + HO_2$	1
J9)	$PAN + h\nu \rightarrow CH_3COO_2 + NO_2$	1
J10)	$CH_3OOH + h\nu \rightarrow CH_2O + OH + HO_2$	1
J11)	$C_2H_5OOH + h\nu \rightarrow CH_3CHO + OH + HO_2$	1
J12)	$C_3H_7OOH + h\nu \rightarrow 0.24\ C_2H_5O_2 + 0.09\ CH_3CHO + 0.18\ CO + 0.7\ CH_3COCH_3 + OH + HO_2$	1
J13)	$CH_3COCH_3 + h\nu \rightarrow CH_3COO_2 + CH_3O_2$	3
J14)	$HOROOH + h\nu \rightarrow 0.25\ CH_3CHO + 1.75\ CH_2O + HO_2 + OH + H_2O$	1
J15)	$CH_3COOOH + h\nu \rightarrow CH_3O_2 + CO_2 + OH$	4
J16)	$CH_2O + h\nu \rightarrow CO + 2\ HO_2$	1
J17)	$CH_2O + h\nu \rightarrow CO + 2\ H_2$	1
J18)	$CH_3CHO + h\nu \rightarrow CH_3O_2 + CO + HO_2$	5
J19)	$ISOOH + h\nu \rightarrow MACR + CH_2O + OH + HO_2$	1
J20)	$ISON + h\nu \rightarrow NO_2 + MACR + CH_2O + HO_2$	1,6,7
J21)	$MACR + h\nu \rightarrow CH_3COO_2 + CH_2O + CO + HO_2$	6,7,8
J22)	$MPAN + h\nu \rightarrow MACRO_2 + NO_2$	1
J23)	$MACROOH + h\nu \rightarrow OH + 0.5\ HACET + 0.5\ CO + 0.5\ MGLY + 0.5\ CH_2O + HO_2$	1
J24)	$HACET + h\nu \rightarrow CH_3COO_2 + CH_2O + HO_2$	1,6
J25)	$MGLY + h\nu \rightarrow CH_3COO_2 + CO + HO_2$	5,6,7
J26)	$NALD + h\nu \rightarrow CH_2O + CO + NO_2 + HO_2$	5

References: 1, *DeMore et al.* [1997]; 2, *Talukdar et al.* [1998]; 3, *Gierczak et al.* [1998]; 4, *Müller and Brasseur* [1995]; 5, *Atkinson et al.* [1999]. 6, *Jenkin et al.* [1997]; 7, *Pöschl et al.* [2000]; 8, *Carter* [1990].

Table 2.3. Chemical Reactions Included in CHASER (Gas/liquid-phase and Heterogeneous Reactions)

No.	Reaction	Rate	Ref.
K1)	$O(^1D) + O_2 \rightarrow O + O_2$	$k_1 = 3.20E\text{-}11\ \exp(70/T)$	1
K2)	$O(^1D) + N_2 \rightarrow O + N_2$	$k_2 = 1.80E\text{-}11\ \exp(110/T)$	1
K3)	$O(^1D) + H_2O \rightarrow 2\ OH$	$k_3 = 2.20E\text{-}10$	1
K4)	$O(^1D) + N_2O \rightarrow 2\ NO$	$k_4 = 6.70E\text{-}11$	1
K5)	$O + O_2 + M \rightarrow O_3 + M$	$k_5 = 6.40E\text{-}34\ \exp(300/T)^{2.3}$	1
K6)	$H_2 + O(^1D) \rightarrow OH + HO_2$	$k_6 = 1.10E\text{-}10$	1
K7)	$H_2 + OH \rightarrow HO_2 + H_2O$	$k_7 = 5.50E\text{-}12\ \exp(-2000/T)$	1
K8)	$O + HO_2 \rightarrow OH + O_2$	$k_8 = 3.00E\text{-}11\ \exp(200/T)$	1
K9)	$O + OH \rightarrow HO_2 + O_2$	$k_9 = 2.20E\text{-}11\ \exp(120/T)$	1
K10)	$O_3 + OH \rightarrow HO_2 + O_2$	$k_{10} = 1.50E\text{-}12\ \exp(-880/T)$	1
K11)	$O_3 + HO_2 \rightarrow OH + 2\ O_2$	$k_{11} = 2.00E\text{-}14\ \exp(-680/T)$	1
K12)	$O + NO_2 \rightarrow NO + O_2$	$k_{12} = 5.60E\text{-}12\ \exp(180/T)$	1

Table 2.3. (continued)

No.	Reaction	Rate	Ref.
K13)	$O_3 + NO \rightarrow NO_2 + O_2$	$k_{13} = 3.00E\text{-}12\ \exp(-1500/T)$	1
K14)	$O_3 + NO_2 \rightarrow NO_3 + O_2$	$k_{14} = 1.20E\text{-}13\ \exp(-2450/T)$	1
K15)	$OH + HO_2 \rightarrow H_2O + O_2$	$k_{15} = 4.80E\text{-}11\ \exp(250/T)$	1
K16)	$OH + H_2O_2 \rightarrow H_2O + HO_2$	$k_{16} = 2.90E\text{-}12\ \exp(-160/T)$	1
K17)	$HO_2 + NO \rightarrow NO_2 + OH$	$k_{17} = 3.50E\text{-}12\ \exp(250/T)$	1
K18)	$HO_2 + HO_2 \rightarrow H_2O_2 + O_2$	$k_{18} = (k_a + k_b\ [M])\ k_c$ $k_a = 2.30E\text{-}13\ \exp(600/T)$ $k_b = 1.70E\text{-}33\ \exp(1000/T)$ $k_c = 1$ $+ 1.40E\text{-}21\ [H_2O]\ \exp(2200/T)$	1
K19)	$OH + NO_2 + M \rightarrow HNO_3 + M$	$k_0 = 2.40E\text{-}30\ (300/T)^{3.1}$ $k_\infty = 1.70E\text{-}11\ (300/T)^{2.1}$ $F_c = 0.6$	1
K20)	$OH + HNO_3 \rightarrow NO_3 + H_2O$	$k_{20} = k_a + k_b\ [M]\ /(1 + k_b\ [M]/k_c)$ $k_a = 2.40E\text{-}14\ \exp(460/T)$ $k_b = 6.50E\text{-}34\ \exp(1335/T)$ $k_c = 2.70E\text{-}17\ \exp(2199/T)$	1
K21)	$NO_2 + NO_3 + M \rightarrow N_2O_5 + M$	$k_0 = 2.00E\text{-}30\ (300/T)^{4.4}$ $k_\infty = 1.40E\text{-}12\ (300/T)^{0.7}$ $F_c = 0.6$	1
K22)	$N_2O_5 + M \rightarrow NO_2 + NO_3 + M$	$k_{22} = k_{21}$ $/(2.70E\text{-}27\ \exp(11000/T))$	1
K23)	$N_2O_5 + H_2O \rightarrow 2\ HNO_3$	$k_{23} = 2.10E\text{-}21$	1
K24)	$NO_3 + NO \rightarrow 2\ NO_2$	$k_{24} = 1.50E\text{-}11\ \exp(170/T)$	1
K25)	$NO_2 + HO_2 + M \rightarrow HNO_4 + M$	$k_0 = 1.80E\text{-}31\ (300/T)^{3.2}$ $k_\infty = 4.70E\text{-}12\ (300/T)^{1.4}$ $F_c = 0.6$	1
K26)	$HNO_4 + M \rightarrow NO_2 + HO_2 + M$	$k_{26} = k_{18}$ $/(2.10E\text{-}27\ \exp(10900/T))$	1
K27)	$HNO_4 + OH \rightarrow NO_2 + H_2O + O_2$	$k_{27} = 1.30E\text{-}12\ \exp(380/T)$	1
	— CH_4 oxidation —		
K28)	$CH_4 + OH \rightarrow CH_3O_2 + H_2O$	$k_{28} = 2.45E\text{-}12\ \exp(-1775/T)$	1
K29)	$CH_4 + O(^1D) \rightarrow CH_3O_2 + OH$	$k_{29} = 1.50E\text{-}10$	2
K30)	$CH_3O_2 + NO \rightarrow CH_2O + NO_2 + HO_2$	$k_{30} = 3.00E\text{-}12\ \exp(280/T)$	1
K31)	$CH_3O_2 + CH_3O_2 \rightarrow 1.8\ CH_2O + 0.6\ HO_2$	$k_{31} = 2.50E\text{-}13\ \exp(190/T)$	1
K32)	$CH_3O_2 + HO_2 \rightarrow CH_3OOH + O_2$	$k_{32} = 3.80E\text{-}13\ \exp(800/T)$	1
K33)	$CH_3OOH + OH \rightarrow 0.7\ CH_3O_2 + 0.3\ CH_2O$ $+ 0.3\ OH + H_2O$	$k_{33} = 3.80E\text{-}12\ \exp(200/T)$	1
K34)	$CH_2O + OH \rightarrow CO + HO_2 + H_2O$	$k_{34} = 1.00E\text{-}11$	1
K35)	$CH_2O + NO_3 \rightarrow HNO_3 + CO + HO_2$	$k_{35} = 6.00E\text{-}13\ \exp(-2058/T)$	3
K36)	$CO + OH \rightarrow CO_2 + HO_2$	$k_{36} = 1.50E\text{-}13\ (1 + 0.6\ P_{atm})$	1
	— C_2H_6 and C_3H_8 oxidation —		
K37)	$C_2H_6 + OH \rightarrow C_2H_5O_2 + H_2O$	$k_{37} = 8.70E\text{-}12\ \exp(-1070/T)$	1
K38)	$C_2H_5O_2 + NO \rightarrow CH_3CHO + NO_2 + HO_2$	$k_{38} = 2.60E\text{-}12\ \exp(365/T)$	1
K39)	$C_2H_5O_2 + HO_2 \rightarrow C_2H_5OOH + O_2$	$k_{39} = 7.50E\text{-}13\ \exp(700/T)$	1
K40)	$C_2H_5O_2 + CH_3O_2 \rightarrow 0.8\ CH_3CHO + 0.6\ HO_2$	$k_{40} = 3.10E\text{-}13$	4
K41)	$C_2H_5OOH + OH \rightarrow 0.286\ C_2H_5O_2$ $+ 0.714\ CH_3CHO + 0.714\ OH + H_2O$	$k_{41} = 1.13E\text{-}11\ \exp(55/T)$	4

Table 2.3. (continued)

No.	Reaction	Rate	Ref.
K42)	$C_3H_8 + OH \rightarrow C_3H_7O_2 + H_2O$	$k_{42} = 1.50E\text{-}17\ T^2\ exp(-44/T)$	4
K43)	$C_3H_7O_2 + NO \rightarrow NO_2 + 0.24\ C_2H_5O_2 + 0.09\ CH_3CHO + 0.18\ CO + 0.7\ CH_3COCH_3 + HO_2$	$k_{43} = 2.60E\text{-}17\ exp(360/T)$	4
K44)	$C_3H_7O_2 + HO_2 \rightarrow C_3H_7OOH + O_2$	$k_{44} = 1.51E\text{-}13\ exp(1300/T)$	4
K45)	$C_3H_7O_2 + CH_3O_2 \rightarrow 0.8\ C_2H_5O_2 + 0.3\ CH_3CHO + 0.6\ CO + 0.2\ CH_3COCH_3 + HO_2$	$k_{45} = 2.00E\text{-}13$	4
K46)	$C_3H_7OOH + OH \rightarrow 0.157\ C_3H_7O_2 + 0.142\ C_2H_5O_2 + 0.053\ CH_3CHO + 0.106\ CO + 0.666\ CH_3COCH_3 + 0.843\ OH + 0.157\ H_2O$	$k_{46} = 2.55E\text{-}11$	4
K47)	$CH_3COCH_3 + OH \rightarrow CH_3COCH_2O_2 + H_2O$	$k_{47} = 5.34E\text{-}18\ T^2\ exp(-230/T)$	4
K48)	$CH_3COCH_2O_2 + NO \rightarrow NO_2 + CH_3COO_2 + CH_2O$	$k_{48} = 2.54E\text{-}12\ exp(360/T)$	4
K49)	$CH_3COCH_2O_2 + NO_3 \rightarrow NO_2 + CH_3COO_2 + CH_2O$	$k_{49} = 2.50E\text{-}12$	4
K50)	$CH_3COCH_2O_2 + HO_2 \rightarrow HACET + O_2$	$k_{50} = 1.36E\text{-}13\ exp(1250/T)$	4
K51)	$HACET + OH \rightarrow 0.323\ CH_3COCH_2O_2 + 0.677\ MGLY + 0.677\ OH$	$k_{51} = 9.20E\text{-}12$	4
	— C_2H_4 and C_3H_6 oxidation —		
K52)	$C_2H_4 + OH + M \rightarrow HOC_2H_4O_2 + M$	$k_0 = 1.00E\text{-}28\ (300/T)^{0.8}$ $k_\infty = 8.80E\text{-}12$ $F_c = 0.6$	1
K53)	$C_2H_4 + O_3 \rightarrow 1.37\ CH_2O + 0.63\ CO + 0.12\ OH + 0.12\ HO_2 + 0.1\ H_2 + 0.2\ CO_2 + 0.4\ H_2O + 0.8\ O_2$	$k_{53} = 1.20E\text{-}14\ exp(-2630/T)$	1
K54)	$HOC_2H_4O_2 + NO \rightarrow NO_2 + HO_2 + 2\ CH_2O$	$k_{54} = 9.00E\text{-}12$	2
K55)	$HOC_2H_4O_2 + HO_2 \rightarrow HOROOH + O_2$	$k_{48} = 6.50E\text{-}13\ exp(650/T)$	5
K56)	$C_3H_6 + OH + M \rightarrow HOC_3H_6O_2 + M$	$k_0 = 8.00E\text{-}27\ (300/T)^{3.5}$ $k_\infty = 3.00E\text{-}11$ $F_c = 0.5$	2
K57)	$C_3H_6 + O_3 \rightarrow 0.5\ CH_2O + 0.5\ CH_3CHO + 0.36\ OH + 0.3\ HO_2 + 0.28\ CH_3O_2 + 0.56\ CO$	$k_{57} = 6.50E\text{-}15\ exp(-1900/T)$	1
K58)	$HOC_3H_6O_2 + NO \rightarrow NO_2 + CH_3CHO + CH_2O + HO_2$	$k_{58} = 9.00E\text{-}12$	2
K59)	$HOC_3H_6O_2 + HO_2 \rightarrow HOROOH + O_2$	$k_{59} = 6.50E\text{-}13\ exp(650/T)$	5
K60)	$HOROOH + OH \rightarrow 0.125\ HOC_2H_4O_2 + 0.023\ HOC_3H_6O_2 + 0.114\ MGLY + 0.114\ CH_3COO_2 + 0.676\ CH_2O + 0.438\ CO + 0.85\ OH + 0.90\ HO_2 + H_2O$	$k_{60} = 3.80E\text{-}12\ exp(200/T)$	5
	— other NMVOCs oxidation —		
K61)	$ONMV + OH \rightarrow 0.3\ C_2H_5O_2 + 0.02\ C_3H_7O_2 + 0.468\ ISO_2 + CH_2O + HO_2 + H_2O$	$k_{61} = 1.55E\text{-}11\ exp(-540/T)$	5
	— acetaldehyde degradation etc. —		
K62)	$CH_3CHO + OH \rightarrow CH_3COO_2 + H_2O$	$k_{62} = 5.60E\text{-}12\ exp(270/T)$	1
K63)	$CH_3CHO + NO_3 \rightarrow CH_3COO_2 + HNO_3$	$k_{63} = 1.40E\text{-}12\ exp(-1900/T)$	1
K64)	$CH_3COO_2 + NO \rightarrow NO_2 + CH_3O_2 + CO_2$	$k_{64} = 5.30E\text{-}12\ exp(360/T)$	1
K65)	$CH_3COO_2 + NO_2 + M \rightarrow PAN + M$	$k_0 = 9.70E\text{-}29\ (300/T)^{5.6}$ $k_\infty = 9.30E\text{-}12\ (300/T)^{1.5}$	1

Table 2.3. (continued)

No.	Reaction	Rate	Ref.
		$F_c = 0.6$	
K66)	$PAN + M \rightarrow CH_3COO_2 + NO_2 + M$	$k_{66} = k_{65}$ /(9.00E-29 exp(14000/T))	1
K67)	$CH_3COO_2 + HO_2 \rightarrow CH_3COOOH + O_2$	$k_{67} = 4.50E\text{-}13\ \exp(1000/T)$ /(1 + 1/(3.30E2 exp(-1430/T)))	1
K68)	$CH_3COO_2 + HO_2 \rightarrow CH_3COOH + O_3$	$k_{68} = 4.50E\text{-}13\ \exp(1000/T)$ /(1 + 3.30E2 exp(-1430/T))	1
K69)	$CH_3COOOH + OH \rightarrow CH_3COO_2 + H_2O$	$k_{69} = 6.85E\text{-}12$	6
K70)	$CH_3COO_2 + CH_3O_2 \rightarrow CH_3O_2 + CH_2O + HO_2 + CO_2 + O_2$	$k_{70} = 1.30E\text{-}12\ \exp(640/T)$ /(1 + 1/(2.20E6 exp(-3820/T)))	1
K71)	$CH_3COO_2 + CH_3O_2 \rightarrow CH_3COOH + CH_2O + O_2$	$k_{71} = 1.30E\text{-}12\ \exp(640/T)$ /(1 + 2.20E6 exp(-3820/T))	1
K72)	$CH_3COO_2 + CH_3COO_2 \rightarrow 2\ CH_3O_2 + 2\ CO_2 + O_2$	$k_{72} = 2.90E\text{-}12\ \exp(500/T)$	1
	— C_5H_8 (Isoprene) and $C_{10}H_{16}$ (Terpene) oxidation —		
K73)	$C_5H_8 + OH \rightarrow ISO_2$	$k_{66} = 2.45E\text{-}11\ \exp(410/T)$	6
K74)	$C_5H_8 + O_3 \rightarrow 0.65\ MACR + 0.58\ CH_2O + 0.1\ MACRO_2 + 0.1\ CH_3COO_2 + 0.08\ CH_3O_2 + 0.28\ HCOOH + 0.14\ CO + 0.09\ H_2O_2 + 0.25\ HO_2 + 0.25\ OH$	$k_{74} = 7.86E\text{-}15\ \exp(-1913/T)$	6
K75)	$C_5H_8 + NO_3 \rightarrow ISON$	$k_{75} = 3.03E\text{-}12\ \exp(-446/T)$	6
K76)	$ISO_2 + NO \rightarrow 0.956\ NO_2 + 0.956\ MACR + 0.956\ CH_2O + 0.956\ HO_2 + 0.044\ ISON$	$k_{76} = 2.54E\text{-}12\ \exp(360/T)$	6
K77)	$ISO_2 + HO_2 \rightarrow ISOOH$	$k_{77} = 2.05E\text{-}13\ \exp(1300/T)$	6
K78)	$ISO_2 + ISO_2 \rightarrow 2\ MACR + CH_2O + HO_2$	$k_{78} = 2.00E\text{-}12$	6
K79)	$ISOOH + OH \rightarrow MACR + OH$	$k_{79} = 1.00E\text{-}10$	6
K80)	$ISON + OH \rightarrow NALD + 0.2\ MGLY + 0.1\ CH_3COO_2 + 0.1\ CH_2O + 0.1\ HO_2$	$k_{80} = 1.30E\text{-}11$	6
K81)	$MACR + OH \rightarrow MACRO_2$	$k_{81} =$ 0.5 (4.13E-12 exp(452/T) + 1.86E-11 exp(175/T))	6
K82)	$MACR + O_3 \rightarrow 0.9\ MGLY + 0.45\ HCOOH + 0.32\ HO_2 + 0.22\ CO + 0.19\ OH + 0.1\ CH_3COO_2$	$k_{82} =$ 0.5 (1.36E-15 exp(-2112/T) + 7.51E-16 exp(-1521/T))	6
K83)	$MACRO_2 + NO \rightarrow NO_2 + 0.25\ HACET + 0.25\ CO + 0.25\ CH_3COO_2 + 0.5\ MGLY + 0.75\ CH_2O + 0.75\ HO_2$	$k_{83} = 2.54E\text{-}12\ \exp(360/T)$	6
K84)	$MACRO_2 + HO_2 \rightarrow MACROOH$	$k_{84} = 1.82E\text{-}13\ \exp(1300/T)$	6
K85)	$MACRO_2 + MACRO_2 \rightarrow HACET + MGLY + 0.5\ CH_2O + 0.5\ CO$	$k_{85} = 2.00E\text{-}12$	6
K86)	$MACRO_2 + NO_2 + M \rightarrow MPAN + M$	$k_0 = 9.70E\text{-}29\ (300/T)^{5.6}$ $k_\infty = 9.30E\text{-}12\ (300/T)^{1.5}$ $F_c = 0.6$	1,6
K87)	$MPAN + M \rightarrow MACRO_2 + NO_2 + M$	$k_{87} = k_{86}$ /(9.00E-29 exp(14000/T))	1,6
K88)	$MPAN + OH \rightarrow NO_2 + 0.2\ MGLY + 0.1\ CH_3COO_2 + 0.1\ CH_2O + 0.1\ HO_2$	$k_{88} = 3.60E\text{-}12$	4
K89)	$MACROOH + OH \rightarrow MACRO_2 + H_2O$	$k_{89} = 3.00E\text{-}11$	6

Table 2.3. (continued)

No.	Reaction	Rate	Ref.
K90)	$MGLY + OH \rightarrow CH_3COO_2 + CO$	$k_{90} = 1.50E\text{-}11$	6
K91)	$MGLY + NO_3 \rightarrow CH_3COO_2 + CO + HNO_3$	$k_{91} = 1.44E\text{-}12\ \exp(-1862/T)$	6
K92)	$NALD + OH \rightarrow CH_2O + CO + NO_2$	$k_{92} = 5.60E\text{-}12\ \exp(270/T)$	6
K93)	$C_{10}H_{16} + OH \rightarrow 1.3\ ISO_2 + 0.6\ CH_3COCH_3$	$k_{93} = 1.20E\text{-}11\ \exp(444/T)$	7
K94)	$C_{10}H_{16} + O_3 \rightarrow 1.3\ MACR + 1.16\ CH_2O + 0.2\ MACRO_2 + 0.2\ CH_3COO_2 + 0.16\ CH_3O_2 + 0.56\ HCOOH + 0.28\ CO + 0.18\ H_2O_2 + 0.5\ HO_2 + 0.5\ OH$	$k_{94} = 9.90E\text{-}16\ \exp(-730/T)$	5
K95)	$C_{10}H_{16} + NO_3 \rightarrow 1.2\ ISO_2 + NO_2$	$k_{95} = 5.60E\text{-}11\ \exp(-650/T)$	5
	— SO_2 oxidation (gas-phase) —		
K96)	$SO_2 + OH + M \rightarrow SO_4 + HO_2 + M$	$k_0 = 3.00E\text{-}31\ (300/T)^{3.3}$ $k_\infty = 1.50E\text{-}12$ $F_c = 0.6$	1
K97)	$SO_2 + O_3 \rightarrow SO_4 + O_2$	$k_{97} = 3.00E\text{-}12\ \exp(-7000/T)$	1
	— DMS oxidation —		
K98)	$DMS + OH \rightarrow CH_3SCH_2O_2 + H_2O$	$k_{98} = 1.20E\text{-}11\ \exp(-260/T)$	1,4
K99)	$DMS + OH \rightarrow SO_2 + 1.2\ CH_3O_2$	$k_{99} = k_a\ \tanh(\ k_b/k_a\ )$ $k_a = 1.8E\text{-}11$ $k_b = 5.2E\text{-}12 + 4.7E\text{-}15\ (T\text{-}315)^2$	1,4
K100)	$CH_3SCH_2O_2 + NO \rightarrow NO_2 + 0.9\ SO_2 + 0.9\ CH_3O_2 + 0.9\ CH_2O$	$k_{100} = 8.00E\text{-}12$	4
K101)	$CH_3SCH_2O_2 + CH_3SCH_2O_2 \rightarrow SO_2 + CH_3O_2 + CH_2O$	$k_{101} = 2.00E\text{-}12$	4
K102)	$DMS + NO_3 \rightarrow SO_2 + HNO_3$	$k_{102} = 1.90E\text{-}13\ \exp(500/T)$	1
	— Heterogeneous reactions [a] *—*		
H1)	$N_2O_5 \rightarrow 2\ HNO_3$	$\gamma_1^{liq} = 0.1,\ \gamma_1^{ice} = 0.01$	8,9
H2)	$HO_2 \rightarrow 0.5\ H_2O_2 + 0.5\ O_2$	$\gamma_2^{liq} = 0.1,\ \gamma_2^{ice} = 0.01$	9
H3)	$HOC_2H_4O_2 \rightarrow HOROOH$	$\gamma_3^{liq} = 0.1,\ \gamma_3^{ice} = 0.01$	9
H4)	$HOC_3H_6O_2 \rightarrow HOROOH$	$\gamma_4^{liq} = 0.1,\ \gamma_4^{ice} = 0.01$	9
H5)	$ISO_2 \rightarrow ISOOH$	$\gamma_5^{liq} = 0.07,\ \gamma_5^{ice} = 0.01$	9
H6)	$MACRO_2 \rightarrow MACROOH$	$\gamma_6^{liq} = 0.07,\ \gamma_6^{ice} = 0.01$	9
H7)	$CH_3COO_2 \rightarrow$ products	$\gamma_7^{liq} = 0.004,\ \gamma_7^{ice} = 0.$	9
	— SO_2 oxidation (liquid-phase) —		
A1)	$S(IV)$ [b] $+ O_3(aq) \rightarrow SO_4$	$l_1(T, [H^+])$ [c]	10
A2)	$S(IV) + H_2O_2(aq) \rightarrow SO_4$	$l_2(T, [H^+])$ [c]	10

T, temperature (K); P_{atm}, pressure (atm); [M], air number density (cm^{-3}); [H_2O], water vapor density (cm^{-3}); The three-body reaction rates are computed by $k = (k_0[M])/(1 + k_0[M]/k_\infty)F_c^{\{1+[\log_{10}(k_0[M]/k_\infty)]^2\}^{-1}}$.
References: 1, *DeMore et al.* [1997]; 2, *Atkinson et al.* [2000]; 3, *Cantrell et al.* [1985]; 4, *Jenkin et al.* [1997]; 5, *Müller and Brasseur* [1995]; 6, *Pöschl et al.* [2000]; 7, *Carter* [1990]; 8, *Dentener and Crutzen* [1993]; 9, *Jacob* [2000]; 10, *Hoffmann and Calvert* [1985].

[a] Considered for liquid-phase aerosols (uptake coefficient γ^{liq}) and ice cloud particles (γ^{ice}).

[b] $S(IV)$ denotes the sum of SO_2(aq), HSO_3^-, and SO_3^{2-} in aqueous phase.

[c] Reaction rate constants as a function of T and $[H^+]$ are given in Appendix 2B (page 106).

is given by the following, according to *Schwartz* [1986], *Dentener and Crutzen* [1993], and *Jacob* [2000].

$$\beta_i = \sum_j \left(\frac{4}{v_i \gamma_{ij}} + \frac{R_j}{D_{ij}} \right)^{-1} \cdot A_j \tag{2.1}$$

where v_i is the mean molecular speed (cm s^{-1}) of the species i (calculated as $\sqrt{8R_gT/(\pi M_i)} \times 10^2$, R_g: the gas constant, T: temperature, M: molecular mass), D_{ij} is the gaseous mass transfer (diffusion) coefficient (cm^2 s^{-1}) of the species i for the particle type j given as a function of the diffusive coefficient for i and the effective radius R_j (cm) for the particle type j [e.g., *Frössling*, 1938; *Perry and Green*, 1984], and A_j are the surface area density (cm^2 cm^{-3}) for the particle type j. In this study, j denotes sulfate aerosol, sea-salt aerosol, and liquid/ice particles in cumulus and large-scale clouds. In a run without sulfate simulation, concentrations of both sulfate and sea-salt are prescribed using the monthly averaged output from the global aerosol model [*Takemura et al.*, 2000] which is also based on the CCSR/NIES AGCM, whereas the model uses sulfate distributions calculated on-line in the model in a run including sulfate simulation (this study). Those concentrations are converted to the surface area densities A_j by assuming the log-normal distributions of particle size with mode radii variable with the relative humidity (RH). In the conversion, an empirical relation of *Tabazadeh et al.* [1997] and *Sander et al.* [2000] is also employed to estimate the weight percentage (%) of H_2SO_4/H_2O (sulfate) aerosol. The effective radius R_j for aerosols is calculated as a function of RH as in the aerosol model of *Takemura et al.* [2000]. In the case of reactions on cloud particles, spatially inhomogeneous distributions of clouds in the model grids should be taken into account in fact, since using the grid averaged surface area densities for clouds would lead to an overestimation of β in Equation 2.1 particularly for radical species with short lifetimes (i.e., due to unrealistic loss outside clouds). In this study, heterogeneous reactions on cloud particles for HO_2 and RO_2 radicals are applied only when the grid cloud fraction in the AGCM is 1 (100% cloud coverage). To estimate the surface area density for cloud particles, the liquid water content (LWC) and ice water content (IWC) in the AGCM are converted using the cloud droplet distribution of *Battan and Reitan* [1957] and the relation between IWC and the surface area density [*McFarquhar and Heymsfield*, 1996; *Lawrence and Crutzen*, 1998] (for ice clouds). In the simulation, Equation 2.1 gives τ ($\equiv 1/\beta$) of 1-5 min for $\gamma = 0.1$ in the polluted boundary layers (e.g., Europe) in accordance with the sulfate distributions, and τ ranging from several hours to a few days in the upper troposphere for $\gamma = 0.1$ (for liquid) and $\gamma = 0.01$ (for ice).

In this study, the model also includes the sulfate formation process with the gas and liquid-phase oxidation of SO_2 and dimethyl sulfide (DMS) as listed in Table 2.3. Details of the SO_2 oxidation in liquid-phase in the model (reaction A1 and A2) are described in Appendix 2B of this chapter (page 106). As described above, simulated sulfate distributions are reflected on-line on the calculation of the heterogeneous loss rates (Equation 2.1).

Reaction rate constants for the reactions listed in Table 2.2 and Table 2.3 are mainly taken from

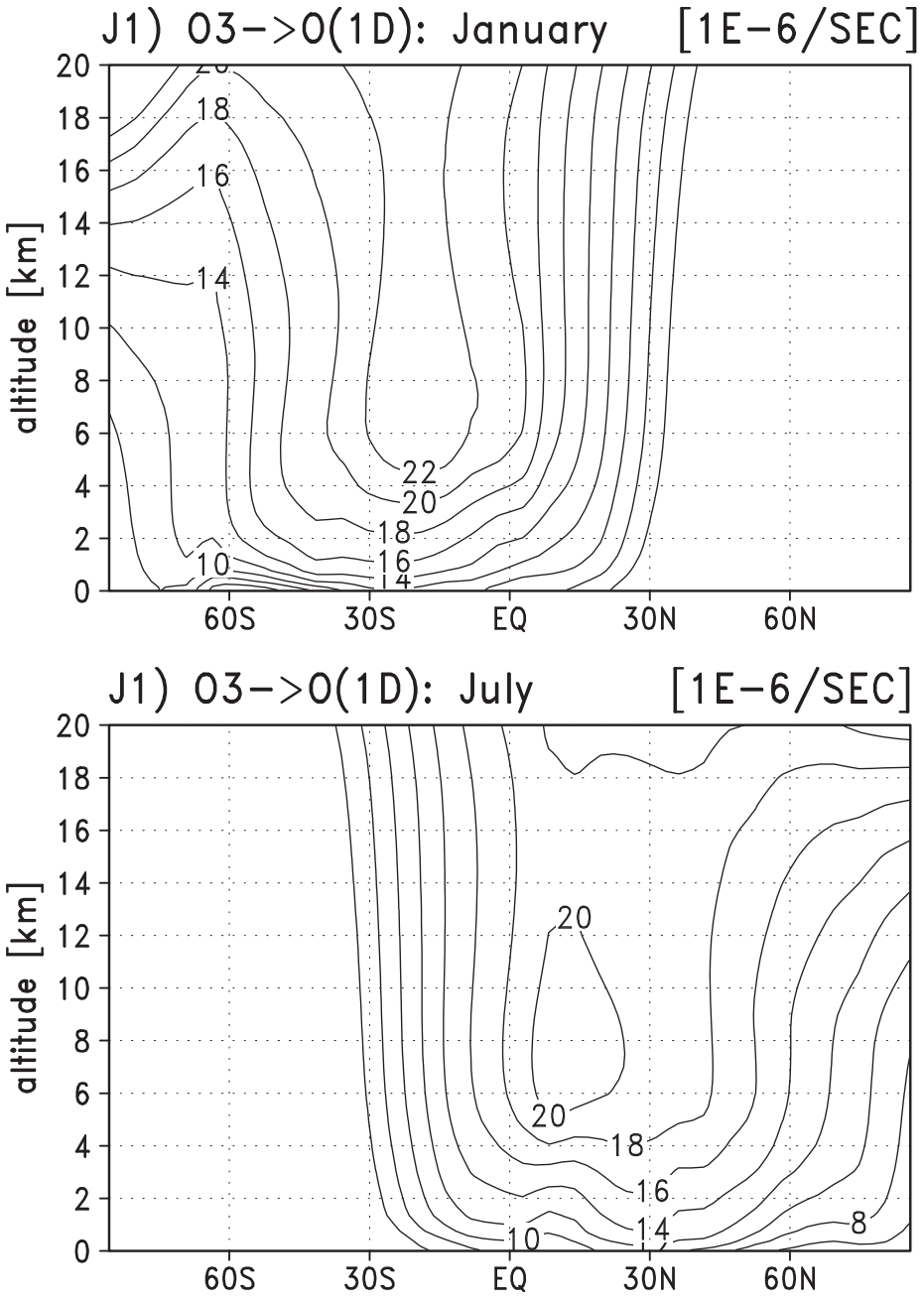

Figure 2.3. Zonally averaged photolysis rate (10^{-6} sec^{-1}) of the O_3 to $O(^1D)$ photolysis calculated for January and July.

DeMore et al. [1997] and *Atkinson et al.* [2000], and *Sander et al.* [2000] for updated reactions. The quantum yield for $O(^1D)$ production in ozone photolysis (J1) is based on *Talukdar et al.* [1998]. The photolysis rates (J-values) are calculated on-line by using temperature and radiation fluxes computed in the radiation component of CHASER. The radiation scheme adopted in CHASER (based on the CCSR/NIES AGCM) considers the absorption and scattering by gases, aerosols and clouds, and the effect of surface albedo. In the CCSR/NIES AGCM, the original wavelength resolution for

the radiation calculation is relatively coarse in the ultraviolet and the visible wavelength regions as in general AGCMs. Therefore, the wavelength resolution in these wavelength regions has been improved for the photochemistry in CHASER. In addition, representative absorption cross sections and quantum yields for individual spectral bins are evaluated depending on the optical thickness computed in the radiation component, in a way similar to *Landgraf and Crutzen* [1998]. The photolysis rate for the $O_3 \rightarrow O(^1D)$ reaction calculated for January and July can be seen in Figure 2.3.

CHASER uses an Euler Backward Iterative (EBI) method to solve the gas-phase chemical reaction system. The method is largely based on *Hertel et al.* [1993] which increases the efficiency of the iteration process by using analytical solutions for strongly coupled species (e.g., OH-HO_2). For liquid-phase reactions, a similar EBI scheme is used to consider the time integration of concentrations in bulk phase (gas+liquid phase; see Appendix 2B, page 106). The chemical equations in both gas and liquid-phase are solved with a time step of 10 min in this study. Configurations of the chemical scheme such as a choice of species, reactions and reaction rates are automatically processed by the preprocessor to set up the model through input files (Figure 2.2). Therefore, the chemical reaction system as listed in Table 2.2 and Table 2.3 can be easily changed by an user.

2.2.2 Emissions

Surface emissions are considered for CO, NO_x, NMHCs, and sulfur species of SO_2 and DMS in this study (Table 2.4). Anthropogenic emissions associated with industry (e.g., fossil fuel combustion) and car traffic are based on the Emission Database for Global Atmospheric Research (EDGAR) Version 2.0 [*Olivier et al.*, 1996]. NMHCs emissions from ocean are taken from *Müller* [1992] as in the MOZART model. In the previous version of CHASER [*Sudo et al.*, 2002a], acetone (CH_3COCH_3) emission from ocean was not taken into account, and underestimation of acetone was found over remote Pacific areas by a factor of 2 [*Sudo et al.*, 2002b]. The model, in this study, includes oceanic acetone emissions amounting to 12 TgC/yr in the global in view of the simulation by *Jacob et al.* [2002]. The geographical distribution of biomass burning is taken from *Hao and Liu* [1994]. The emission rates of NMHCs by biomass burning were generally scaled to the values adopted in the MOZART model [*Brasseur et al.*, 1998]. The active fire (Hot Spot) data derived from Advanced Very High Resolution Radiometer (AVHRR) and Along Track Scanning Radiometer (ATSR) [*Arino et al.*, 1999] are used as a scaling factor to simulate the seasonal variation of biomass burning emissions. In this study, we estimated the timing of biomass burning emissions, using the hot spot data for 1999 derived from ATSR. We assumed that individual daily hot spots in a model grid cause emissions which decline in a time scale of 20 days in that grid. The temporal resolution for biomass burning emissions is 10 days in this study. Simulated biomass burning emissions in South America have peaks in late August and September (e.g., CO emission, Figure 2.4). In South Africa, biomass burning emissions begin in May or June near the equator and shift southward with having a peak in October, whereas they begin in July in South America. Consequently,

Table 2.4. Global Emissions of Trace Gases Considered in CHASER

	Indu.[a]	B.B[b]	Vegi.[c]	Ocean	Soil	Ligh.[d]	Airc.[e]	Volc.[f]	Total
NO_x	23.10	10.19	0.00	0.00	5.50	5.00[g]	0.55	0.00	44.34
CO	337.40	929.17	0.00	0.00	0.00	0.00	0.00	0.00	1266.57
C_2H_6	3.16	6.62	1.20	0.10	0.00	0.00	0.00	0.00	11.80
C_3H_8	5.98	2.53	1.60	0.11	0.00	0.00	0.00	0.00	10.22
C_2H_4	2.01	16.50	4.30	2.76	0.00	0.00	0.00	0.00	25.57
C_3H_6	0.86	7.38	1.20	3.36	0.00	0.00	0.00	0.00	12.80
CH_3COCH_3	1.02	4.88	11.20	12.00	0.00	0.00	0.00	0.00	29.10
ONMV	34.30	17.84	20.00	4.00	0.00	0.00	0.00	0.00	76.14
C_5H_8	0.00	0.00	400.00	0.00	0.00	0.00	0.00	0.00	400.00
$C_{10}H_{16}$	0.00	0.00	102.00	0.00	0.00	0.00	0.00	0.00	102.00
SO_2	71.83	2.64	0.00	0.00	0.00	0.00	0.09	4.80	79.41
DMS	0.00	0.00	0.00	14.93[g]	0.00	0.00	0.00	0.00	14.93

Units are TgN/yr for NO_x, TgCO/yr for CO, TgC/yr for NMHCs., and TgS/yr for SO_2 and DMS.
[a]Industry.
[b]Biomass Burning.
[c]Vegetaion.
[d]Lightning NO_x.
[e]Aircraft.
[f]Volcanic.
[g]Calculated in the model (see the text).

biomass burning emissions in South America are concentrated in August and September in comparison to South Africa. In South America, surface CO concentrations calculated by using this biomass burning emission seasonality have their peaks in September (see section 2.3.1), in good agreement with observations in South America. CO has industrial emission sources as well as biomass burning emission. Figure 2.5 shows the distribution of CO surface emission for three distinct seasons. Large CO emission is found in industrial regions (principally America, Europe, China, and India) as well as emissions of other trace gases. Biomass burning emission is most intensive in North Africa (January), in South America, and South Africa (September-October) as also seen in Figure 2.4. In April, large emission is found in southeastern Asia in accordance with biomass burning around the Thailand and northern India. In addition to surface emission, there are indirect CO sources from the oxidation of methane and NMHCs (computed in the model). The global CO source from the methane and NMHCs oxidation is estimated at 1514 Tg/yr in CHASER (the detailed budget of the tropospheric CO in CHASER is shown in section 2.3.1).

For NO_x, emissions from aircraft and lightning are considered as well as surface emission. Data for aircraft NO_x emission (0.55 TgN/yr) are taken from the EDGAR inventory. It is assumed that lightning NO_x production amounts to 5.0 TgN/yr in this study. In CHASER, lightning NO_x production is calculated in each time step using the parameterization of *Price and Rind* [1992] linked to the convection scheme of the AGCM. In the model, lightning flash frequencies in clouds are calculated

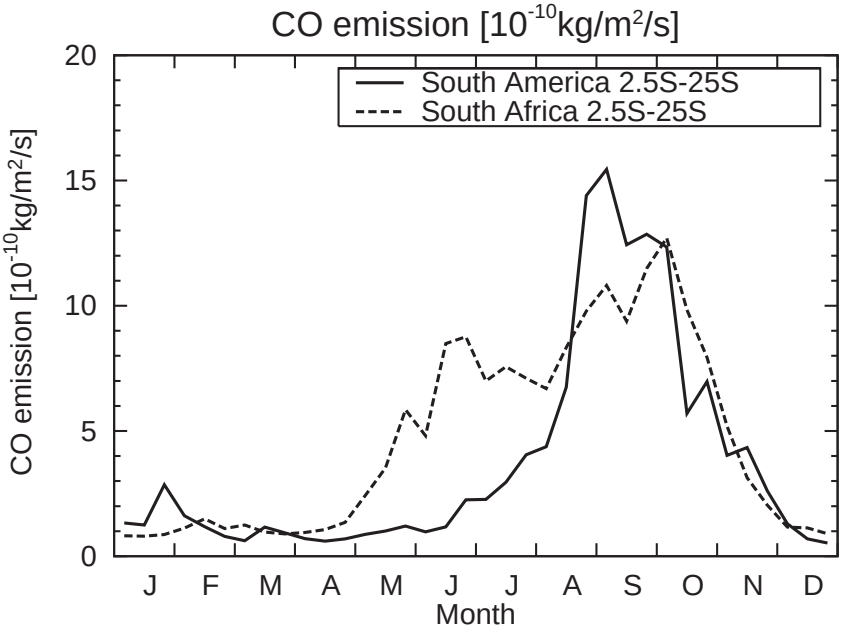

Figure 2.4. Seasonal variations of CO surface emission averaged over South America (2.5°S-25°S) and South Africa (2.5°S-25°S) in the model.

with using the cloud-top height (H) determined from the AGCM convection, and are assumed to be proportional to $H^{4.92}$ and $H^{1.73}$ for continental and marine convective clouds, respectively. The proportions of could-to-ground (CG) flashes and intracloud (IC) flashes (CG/IC) are also calculated with H, following *Price et al.* [1997] (NO_x production by CG flashes is assumed to be 10 times as efficient as by IC flashes). Computed lightning NO_x emission is redistributed vertically by updrafts and downdrafts in the AGCM convection scheme after distributed uniformally in the vertical. As a consequence, computed lightning NO_x emission is transported to the upper tropospheric layers and fractionally to the lower layers in the model (leading to C-shape profiles) as studied by *Pickering et al.* [1998]. The distributions of aircraft and lightning NO_x emissions in the model are shown in Figure 2.6. The aircraft emission seems to have an importance for the NO_x budget in the northern mid-high latitudes especially in wintertime. The lightning emission is generally intense over the continents in the summer-hemisphere. In July, lightning NO_x production is most intensive in the monsoon region like southeastern Asia and North Africa where convective activity is high in this season. NO_x also has an emission source from soils (5.5 TgN/yr) in the model. Soil NO_x emission is prescribed using monthly data for soil NO_x emission from *Yienger and Levy* [1995], obtained via the Global Emissions Inventory Activity (GEIA) [*Graedel et al.*, 1993].

Biogenic emissions from vegetation are considered for NMHCs. The monthly data by *Guenther et al.* [1995], obtained via the GEIA inventory, are used for isoprene, terpenes, ONMV, and other NMHCs emissions. Isoprene emission and terpenes emission are reduced by 20% to 400 TgC/yr and 102 TgC/yr respectively following *Houweling et al.* [1998] and *Roelofs and Lelieveld*

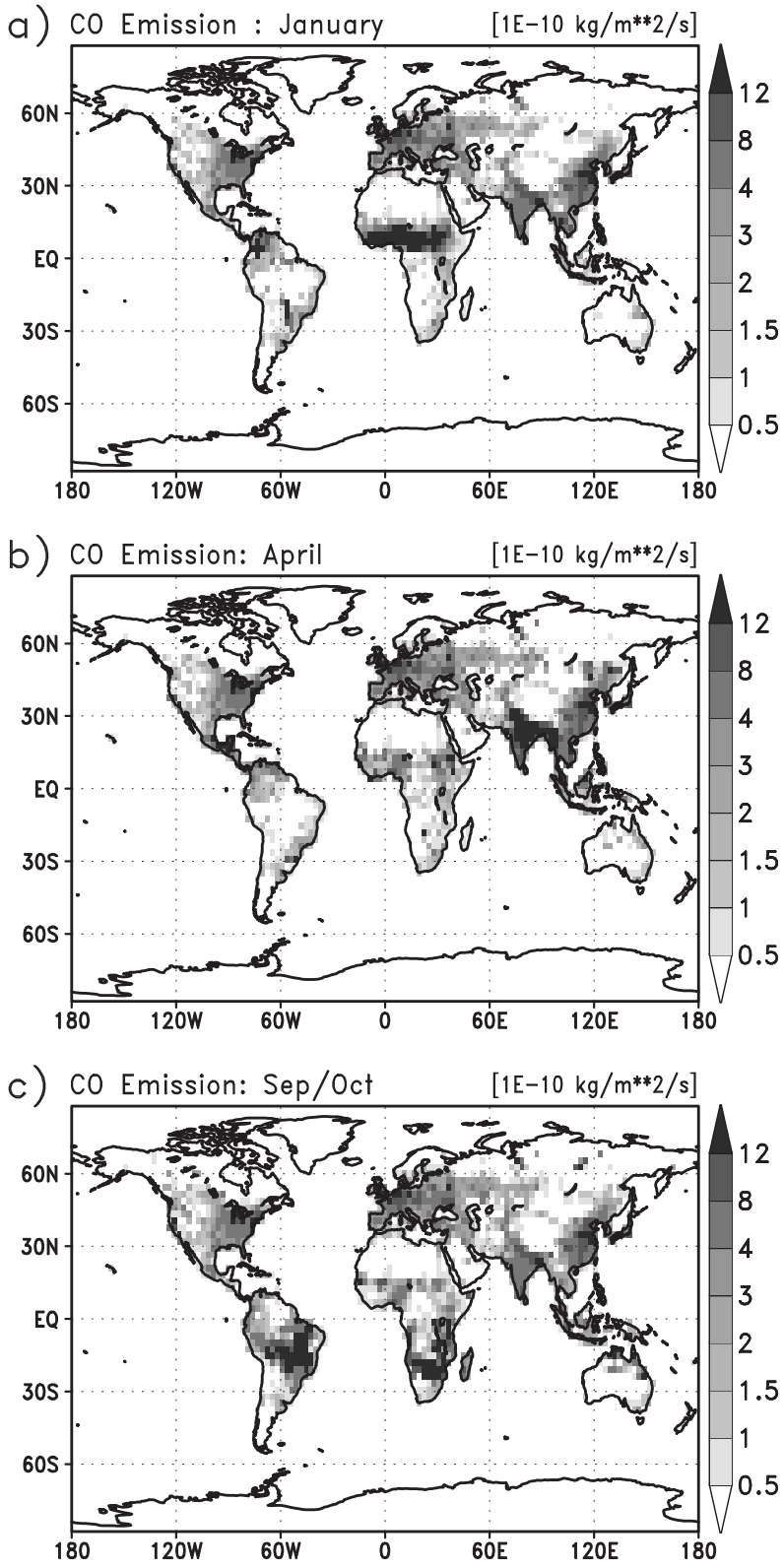

Figure 2.5. Distributions of CO surface emission (10^{-10} kg m^{-2} s^{-1}) considered in the model in January (a), July (b), and September-October (c) average.

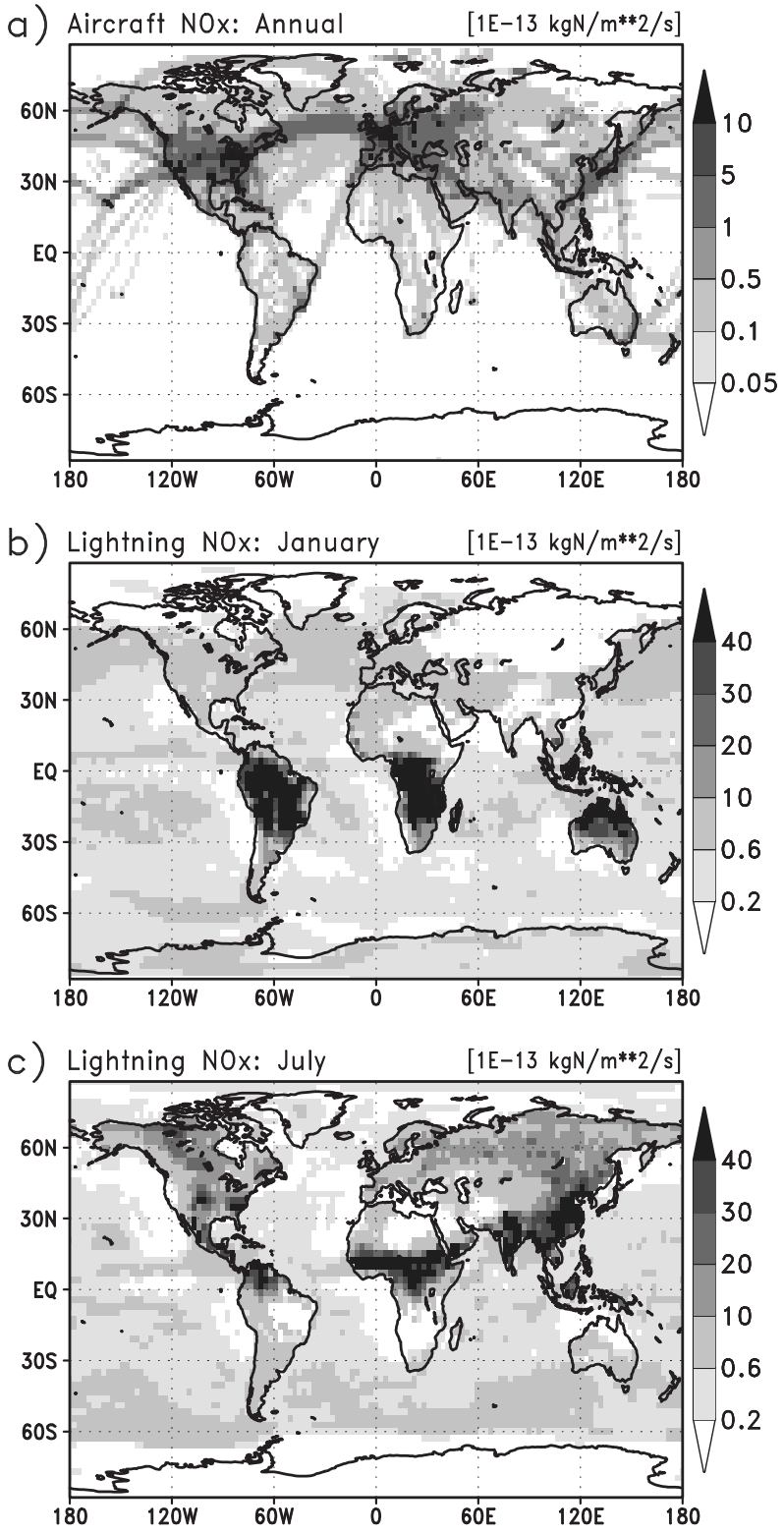

Figure 2.6. Distributions of aircraft and lightning NO_x emission (column total) in CHASER. (a) Aircraft emission (annual mean). (b), (c) lightning emission calculated for January and July respectively.

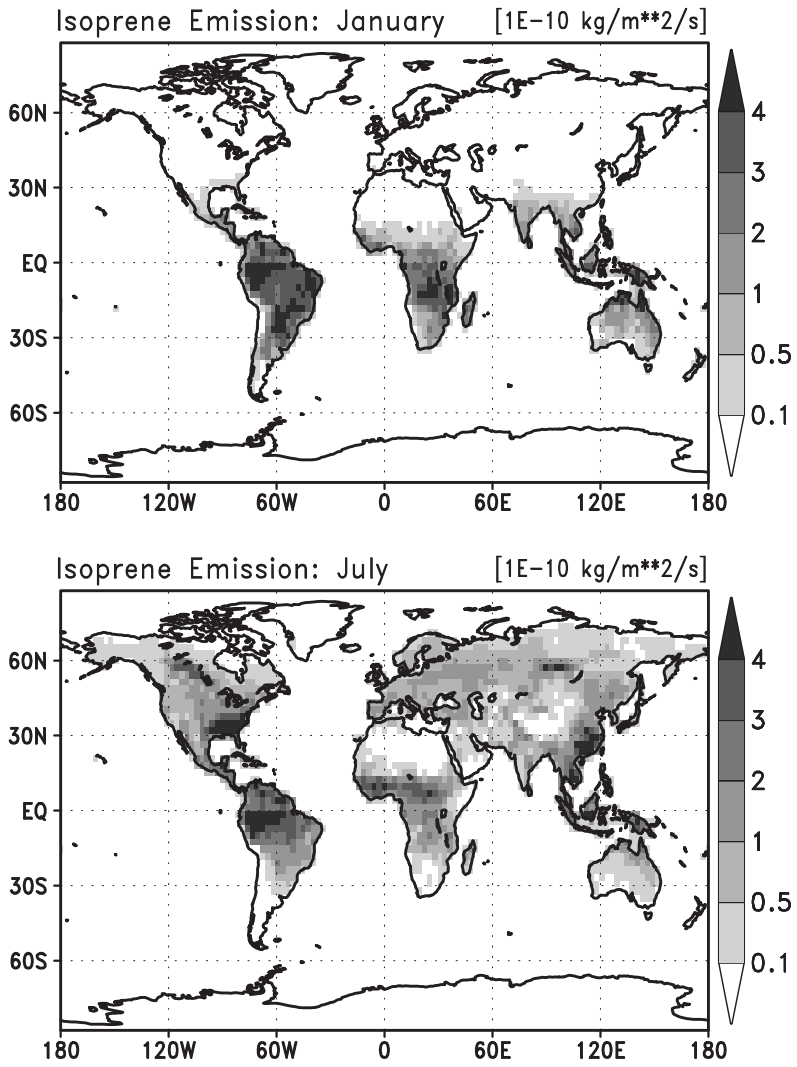

Figure 2.7. Distributions of isoprene (C_5H_8) surface emission for January and July.

[2000]. The diurnal cycle of isoprene emission is simulated using solar incidence at the surface. For terpenes emission, the diurnal cycle is parameterized using surface air temperature in the model [*Guenther et al.*, 1995]. Figure 2.7 shows the distributions of isoprene emission for January and July in the model. Isoprene emission is dominantly large in the tropical region through a year as well as other biogenic NMHCs emissions. In July, isoprene emission is large through much of the continent in the northern hemisphere, with showing significant values in the eastern United States and eastern Asia.

For the sulfate simulation, SO_2 emissions from industry, biomass burning, volcanos, and aircraft are considered using the EDGAR and GEIA database [*Olivier et al.*, 1996; *Andres and Kasgnoc*, 1998], with DMS emission from ocean. As in the aerosol model of *Takemura et al.* [2000], the DMS flux from ocean F_{DMS} (kg $\mathrm{m}^{-2}s^{-1}$) is given as a function of the downward solar flux F_{S} (W

m^{-2}) at the surface, using the following simple parameterization [*Bates et al.*, 1987].

$$F_{\mathrm{DMS}} = 3.56 \times 10^{-13} + 1.08 \times 10^{-14} \times F_{\mathrm{S}} \tag{2.2}$$

This applies to the ocean grids with no sea ice cover in the model. Note that this parameterization ignores other factors controlling the DMS flux such as distribution of planktonic bacteria [e.g., *Six and Maier-Reimer*, 1996].

2.2.3 Deposition

Deposition processes significantly affect the distribution and budget of trace gas species (e.g., O_3, NO_x, HO_x). The CHASER model considers dry deposition at the surface and wet scavenging by precipitation.

Dry deposition

In CHASER, dry deposition scheme is largely based on a resistance series parameterization of *Wesely* [1989] and applied for ozone (O_x), NO_x, HNO_3, HNO_4, PAN, MPAN, ISON, H_2O_2, CO, CH_3COCH_3, CH_2O, MGLY, MACR, HACET, SO_2, DMS, SO_4 and peroxides like CH_3OOH (see Table 2.1) in this study. Dry deposition velocities (v_d) for the lowermost level of the model are computed as

$$v_d = \frac{1}{r_a + r_b + r_s} \tag{2.3}$$

where r_a, r_b, r_s are the aerodynamic resistance, the surface canopy (quasi-laminar) layer resistance, and the surface resistance respectively. r_a has no species dependency and is calculated using surface windspeed and bulk coefficient computed for the model's lowest level in the AGCM. r_b is calculated using friction velocity computed in the AGCM and the Shumid number (calculated with the kinematic viscosity of air and the diffusive coefficient for individual species). Finally, the most important resistance r_s is calculated as a function of surface (vegetation) type over land and species using temperature, solar influx, precipitation, snow cover ratio, and the effective Henry's law constant calculated for individual species in the AGCM. r_s over sea and ice surface are taken to be the values used in *Brasseur et al.* [1998] (e.g., $v_d(\mathrm{O_3})$ = 0.075 cm s^{-1} over sea and ice). The above parameterization, for gaseous species, can not apply for sulfate aerosol (SO_4). In this study, deposition of SO_4 is simulated using a constant velocity v_d of 0.1 (cm s^{-1}). The effect of dry deposition on the concentration of each species in the lowest layer is evaluated together with surface emissions and vertical diffusion by solving the diffusion equations implicitly.

Figure 2.8 shows the calculated 24-hour average deposition velocities (cm s^{-1}) of ozone in January and July. The values show the deposition velocities calculated for the surface elevation. Deposition velocities of ozone are generally higher than 0.1 cm s^{-1}, except for the high latitudes in winter where solar influx is less intense and much of the surface is covered with snow. In July, ozone deposition velocity ranges from 0.2 to 0.5 cm s^{-1} over land surface in the northern

hemisphere (0.3-0.7 cm s^{-1} in daytime), in good agreement with the observations [*Van Pul*, 1992; *Ritter et al.*, 1994; *Jacob et al.*, 1992; *Massman et al.*, 1994]. In the tropical rain forest region (e.g., the Amazon Forest), deposition velocities are high with a range of 0.7-1.2 cm s^{-1} throughout a year, in agreement with the observations [*Fan et al.*, 1990].

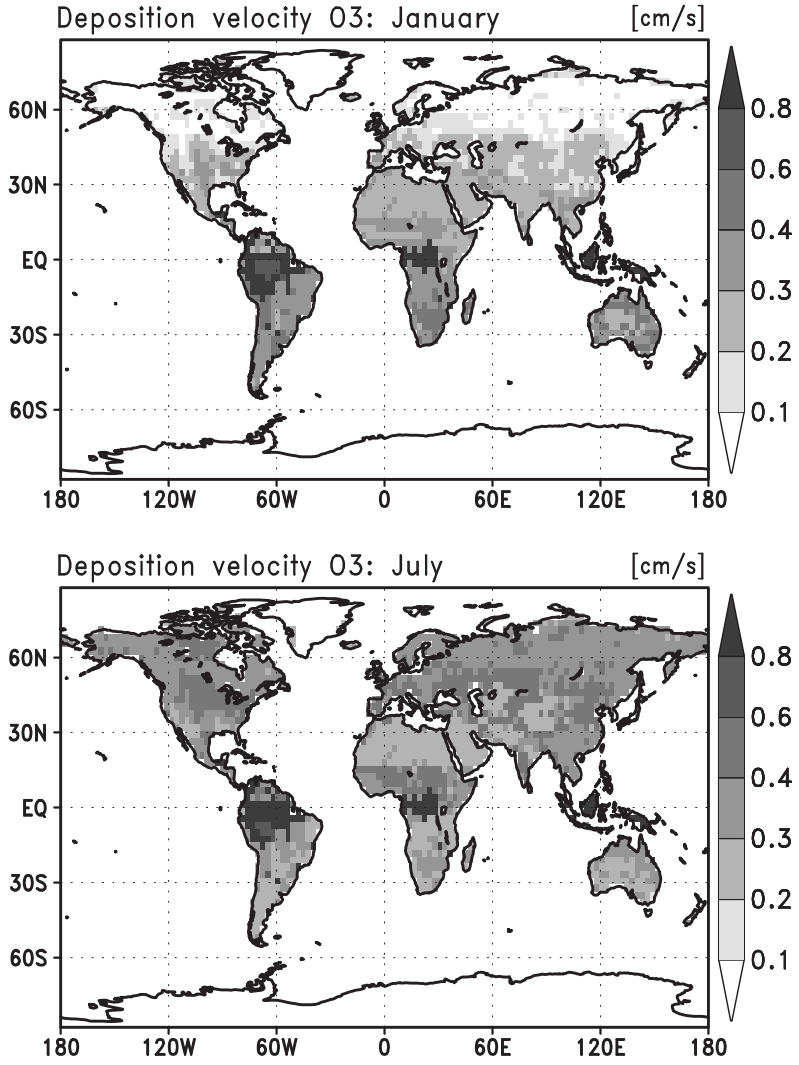

Figure 2.8. Calculated 24-hour average deposition velocities (cm/s) for ozone at the surface in January and July.

Wet deposition

Wet deposition due to large-scale condensation and convective precipitation is considered in two different ways in the model; in-cloud scavenging (rain-out) and below-cloud scavenging (wash-out). A choice of gaseous species which are subject to wet deposition is determined from their effective Henry's law constant in standard conditions (H_s, $T = 298.15$ K). In the present model configuration, wet deposition is applied for species whose H_s are greater than 10^2 M atm^{-1} for both in-cloud and below-cloud scavenging. In this study, the model considers wet deposition for HNO_3, HNO_4, CH_2O, MGLY, HACET, ISON, SO_2, SO_4 and peroxides (H_2O_2, CH_3OOH, etc.), Note that the wet deposition scheme in the previous version of CHASER [*Sudo et al.*, 2002a] does not separate liquid and ice precipitations and ignores the reemission process of dissolved species to the atmosphere, assuming irreversible scavenging. Those processes are newly included in this study as described in the following.

For in-cloud scavenging, the first-order parameterization of *Giorgi and Chameides* [1985] is employed and is extended to incorporate deposition on ice particles. The scheme consists of three processes; deposition associated with liquid precipitation (scavenging loss rate β_l, s^{-1}), with ice precipitation (β_i), and with gravitational settling of ice particles in cirrus clouds (β_s). In this study, deposition on ice particles (i.e., β_i and β_s) is considered only for HNO_3 and H_2O_2. The total loss rate β due to in-cloud scavenging is given by:

$$\beta = \beta_l + \beta_i + \beta_s, \tag{2.4}$$

where

$$\beta_l = \frac{W_l \cdot HRT}{1 + L \cdot HRT + I \cdot K_i} \tag{2.5}$$

$$\beta_i = \frac{W_i \cdot K_i}{1 + L \cdot HRT + I \cdot K_i} \tag{2.6}$$

$$\beta_s = \frac{W_s \cdot K_i}{1 + L \cdot HRT + I \cdot K_i} \tag{2.7}$$

with L and I the liquid and ice water contents (g cm^{-3}), H the effective Henry's law constant, R the gas constant, K_i the ice/gas partitioning coefficient, W_l, W_i and W_s the tendencies (g cm^{-3} s^{-1}) for liquid precipitation, ice precipitation (snow), and gravitational settling of ice particles, respectively. L, I, W_l, W_i, and W_s are computed with respect to convective and large-scale clouds in the AGCM. The tendency due to cloud particle settling W_s are calculated with the terminal velocities of ice cloud particles estimated as a function of I [*Lawrence and Crutzen*, 1998]. The ice/gas uptake partitioning coefficient K_i for H_2O_2 is calculated as a function of temperature according to *Lawrence and Crutzen* [1998]. For HNO_3, K_i is taken to be a large value ($> 10^{10}$), assuming efficient HNO_3 uptake on ice surface. The downward flux of ice-soluble species (HNO_3 and H_2O_2 in this study) associated with cloud gravitational settling (β_s) is treated as a gas-phase flux and is reevaluated in the model grids below clouds.

In the case of below-cloud scavenging, reversible scavenging is considered, which allows reemission of species dissolved in raindrops or precipitating particles to the atmosphere. The tendency of gas-phase concentrations in the ambient atmosphere C_g (g cm^{-3}) due to below-cloud scavenging is given by:

$$\frac{dC_g}{dt} = -K_g(d) \cdot S_p \cdot (C_g - C_e) \tag{2.8}$$

with d the raindrop size (cm) calculated according to *Mason* [1971] and *Roelofs and Lelieveld* [1995], K_g the mass transfer coefficient of a gaseous molecule to a drop calculated by an empirical correlation [e.g., *Frössling*, 1938] as a function of the raindrop size d, the kinematic viscosity of air, the diffusive coefficients, and the terminal velocity of raindrops computed using an empirical relation to d, S_p the surface area density (cm^2/cm^3) of raindrop in the atmosphere, C_e the gas-phase concentration (g cm^{-3}) on the drop surface in equilibrium with the aqueous-phase concentration. The equilibrium concentration C_e is given as:

$$C_e = \frac{C}{HRT} \tag{2.9}$$

with C the aqueous-phase concentration in raindrops (g cm^{-3}) calculated by:

$$C = \frac{F}{P} \tag{2.10}$$

with P the precipitation flux (g cm^{-2} s^{-1}) of rain, and F the flux (g cm^{-2} s^{-1}) of the species dissolved in raindrops (i.e., deposition flux of the species originating from scavenging in the above layers). For the tendency of the ambient mixing ratio Q (g g^{-1}) in the model grids, Eq. 2.8 can be rewritten as:

$$\frac{dQ}{dt} = -\beta_Q (Q - Q_e) \tag{2.11}$$

where $\beta_Q \equiv K_g S_p$ is the scavenging or reemission rate, and Q_e is the equilibrium mixing ratio given by:

$$Q_e = \frac{C}{\rho HRT} = \frac{F}{\rho PHRT} \tag{2.12}$$

with ρ the atmospheric density (g cm^{-3}). Assuming a spherical raindrop, S_p is given as:

$$S_p = L_p \frac{6}{d} \tag{2.13}$$

with L_p the raindrop density (g cm^{-3}) determined from the precipitation flux and the terminal velocity of raindrops, and thereby β_Q is calculated as:

$$\beta_Q = K_g S_p = \frac{6 L_p K_g}{d} \tag{2.14}$$

In the actual scheme, the above calculated β_Q is modified to meet the following mass conservation between C_g (gas-phase) and C (aqueous-phase).

$$\frac{dC_g}{dt} + L_p \frac{dC}{dt} = 0 \tag{2.15}$$

The same type of calculation can apply also for ice precipitation (snow), using K_i and I instead of HRT and L, respectively. The terminal velocity of snowflakes is calculated following *Lawrence and Crutzen* [1998]. In this study, below-cloud scavenging due to ice precipitation is applied only for HNO_3 and H_2O_2 using K_i as used for in-cloud scavenging. For HNO_3, a highly soluble species ($H > 10^{10}$ M atm^{-1}), Q_e is generally calculated to be much small relative to Q ($Q_e \ll Q$), which leads to irreversible scavenging. For moderately soluble species like CH_2O and peroxides, reemission from raindrops ($Q_e > Q$ in Eq. 2.11) is calculated near the surface in the model. In the case of particulate species (SO_4 in this study), below-cloud scavenging is evaluated using the following first-order loss rate:

$$\beta = E\frac{\pi}{4}(d+d_a)^2(v_p - v_a)N_p \tag{2.16}$$

with E the collision efficiency as a function of d, d_a the aerosol particle diameter (cm), v_p and v_a the terminal velocities of raindrops and aerosol particles, and N_p the raindrop number density (cm^{-3}). The aerosol particle diameter d_a is calculated depending on RH in the model. The terminal velocity v_a is estimated by the Stokes's law with a slip correction factor [*Allen and Raabe*, 1982]:

$$v_a = \frac{g\rho_a d^2}{18\eta}\cdot\left[1+2\frac{\lambda}{d_a}\left(1.21+0.4\exp\left(-0.39\frac{d_a}{\lambda}\right)\right)\right] \tag{2.17}$$

where ρ_a is the aerosol density, η and λ are the viscosity and mean free path of air, and g is the gravitational acceleration. This calculation of v_a is also used for the gravitational settling process of aerosol particles in the model. For both gaseous and particulate species, the model also considers the reemission process of dissolved species due to reevaporation of rain or snow in the falling path.

With the above described schemes for in-cloud and below-cloud scavenging, concentrations of individual species dissolved in precipitation are predicted in the model as by Eq 2.10. Figure 2.9 displays the contributions by HNO_3 and SO_4 deposition to the pH value in precipitation (i.e., effect on acid rain) calculated at the surface for January. The contributions are calculated as:

$$\mathrm{pA_N} = -\log[\mathrm{NO_3^-}] \tag{2.18}$$

$$\mathrm{pA_S} = -\log[\mathrm{SO_4^{2-}}] \tag{2.19}$$

using the concentrations (eq l^{-1}) of HNO_3 and SO_4 ($[NO_3^-], [SO_4^{2-}]$) in precipitation as with pH ($\equiv -\log[H^+]$). The contribution by SO_4 deposition (pA_S) appears to be generally larger than that by HNO_3 deposition (pA_N), with showing 4.3-4.0 in the polluted areas around Europe and eastern Asia. Relatively low values of pA_N (4.8-5.0) in the northern high latitudes are due partly to HNO_3 deposition associated with precipitation and sedimentation of ice particles from the upper troposphere and the lower stratosphere. If $[SO_4^{2-}]$ is assumed to be neutralized by cations such as Ca^{2+}, Mg^{2+}, and NH_3^+ in precipitation, pH is estimated as pA_N. On this assumption, the distribution of precipitation pH ($\equiv pA_N$) derived from this simulation (i.e., Figure 2.9a) is well comparable with the estimation by the WMO [*Whelpdale and Miller*, 1989].

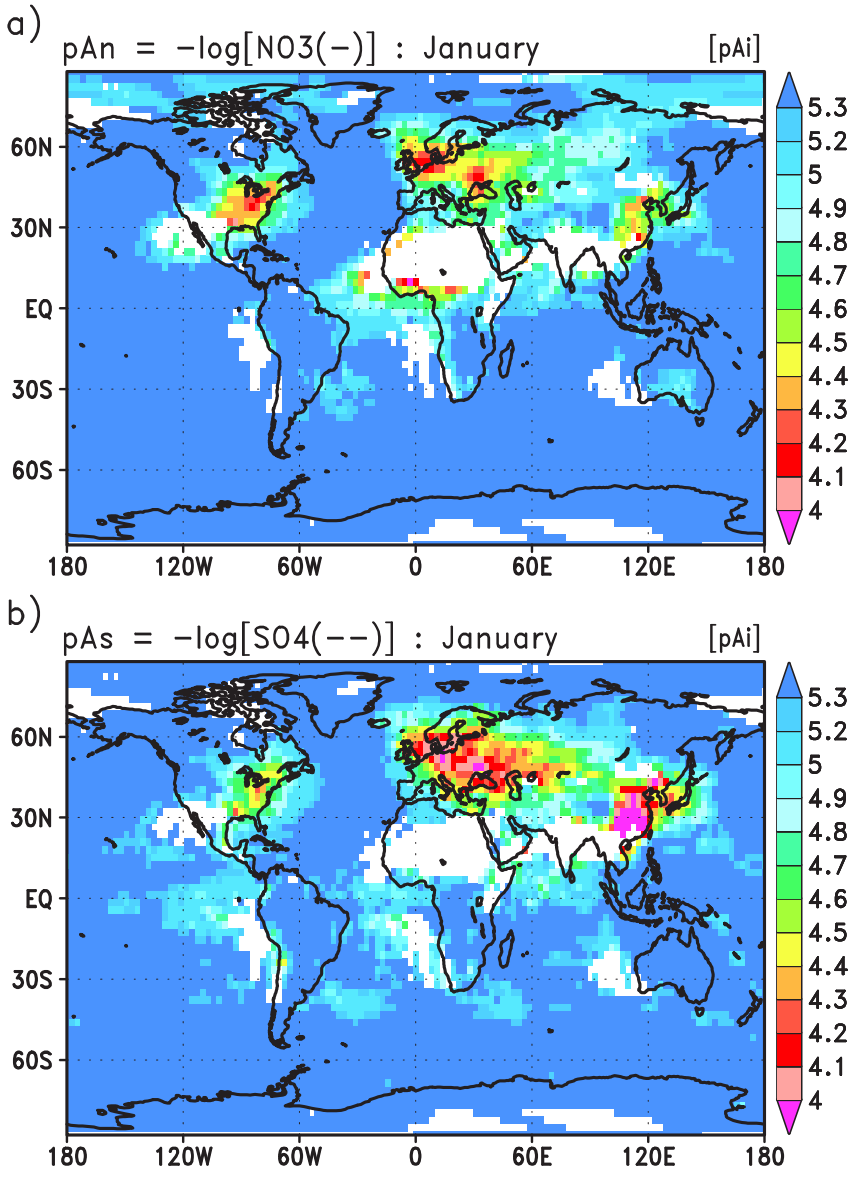

Figure 2.9. Simulated distributions of (a) $pA_N(=-\log[NO_3^-])$ and (b) $pA_S(=-\log[SO_4^{2-}])$ in precipitation to show the contribution by HNO_3 and SO_4 deposition to precipitation pH in the model (for January). Shown are averages volume-weighed with precipitation amount.

The simulated concentrations of nitrates (NO_3^-) and sulfate (SO_4^{2-}) in precipitation are also evaluated with the observation operated by the EMEP network. Figure 2.10 and 2.11 compare the simulated and observed seasonal variation of NO_3^- (mgN l^{-1}) and SO_4^{2-} (mgS l^{-1}) in precipitation for the EMEP sites (during 1978-1995). Both compare concentrations of NO_3^- and SO_4^{2-} volume-weighed with precipitation amount for every month. For both NO_3^- and SO_4^{2-}, the model well captures the observed concentrations, calculating 0-1 mgN l^{-1} for NO_3^- and 0-2 mgS l^{-1} for SO_4^{2-}. The calculation generally shows higher variabilities (indicated by boxes) in winter for both NO_3^- and SO_4^{2-}. The same kind of comparison is also made for wet deposition flux of NO_3^- and SO_4^{2-} with the EMEP data (Figure 2.12 and 2.13). The modeled deposition flux appears to be well comparable with the observation, showing ranges of 0.1-0.5 kgN ha^{-1} month^{-1} for NO_3^- and 0.1-1 kgS ha^{-1} month^{-1} for SO_4^{2-}. The model generally captures the observed seasonal variation associated with chemical production of nitric acid (HNO_3) and sulfate (SO_4^{2-}) and with precipitation. The simulated wet deposition flux in the day-to-day calculations is highly variable (indicated by boxes in the figures) as well as the large annual variation of the observation (error bars). The agreement between the simulation and observation appears to imply successful simulation of the deposition scheme adopted in this study. It should be, however, noted that the above comparisons depend much on precipitation itself simulated by the GCM. Further evaluation of precipitation is needed to validate the nitrates and sulfate simulation in this study (see section 2.3.2 and section 2.3.5 for the simulation of HNO_3 and sulfate).

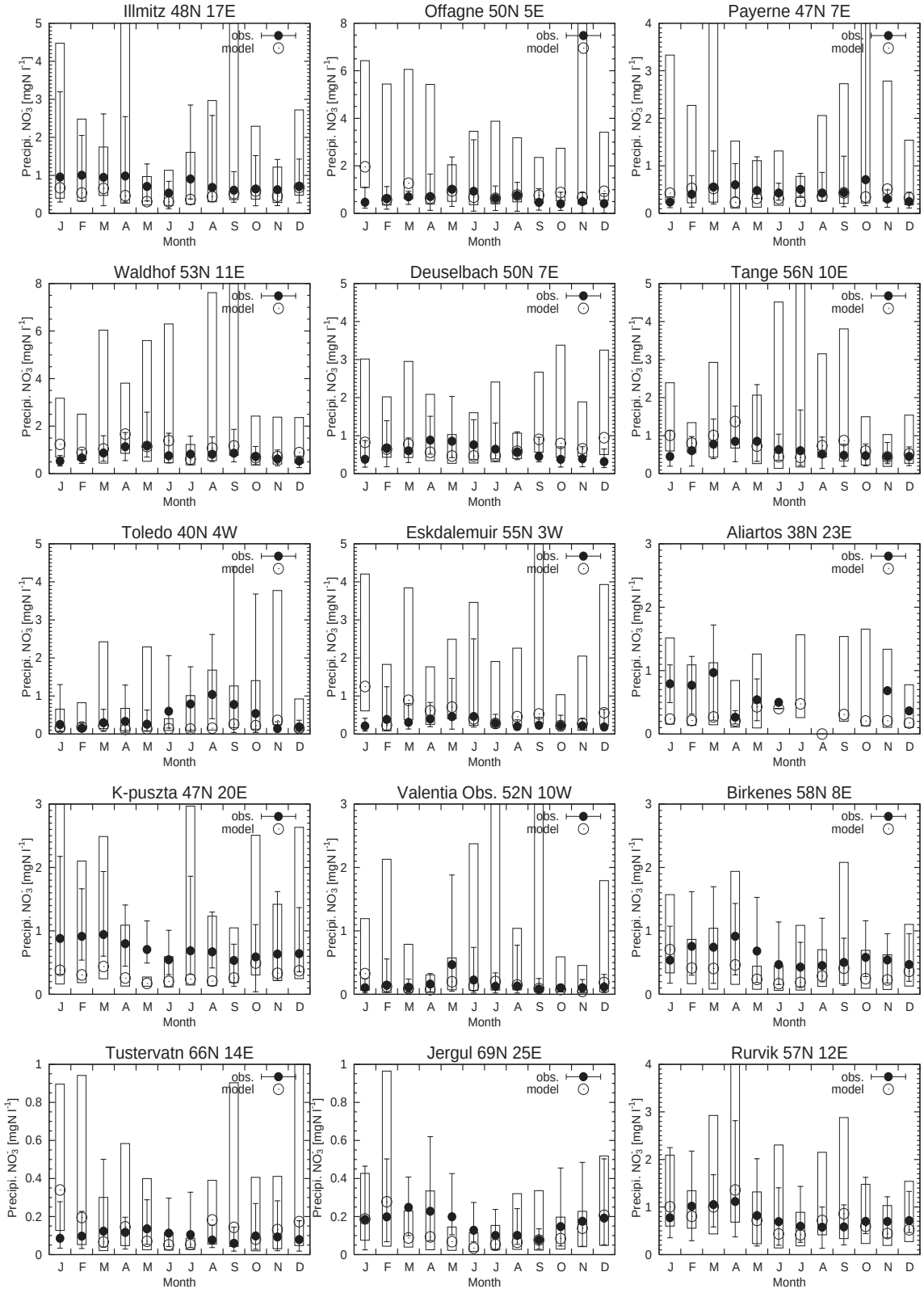

Figure 2.10. Seasonal variations of NO_3^- in precipitation (mgN l^{-1}) observed (solid circles) and calculated (open circles with boxes showing the range) at the surface sites. Both the observations and calculations are volume-weighed with precipitation amount. The ranges of annual variation of the observation (during 1978-1995) are also shown with error bars. The observations are taken from the EMEP network.

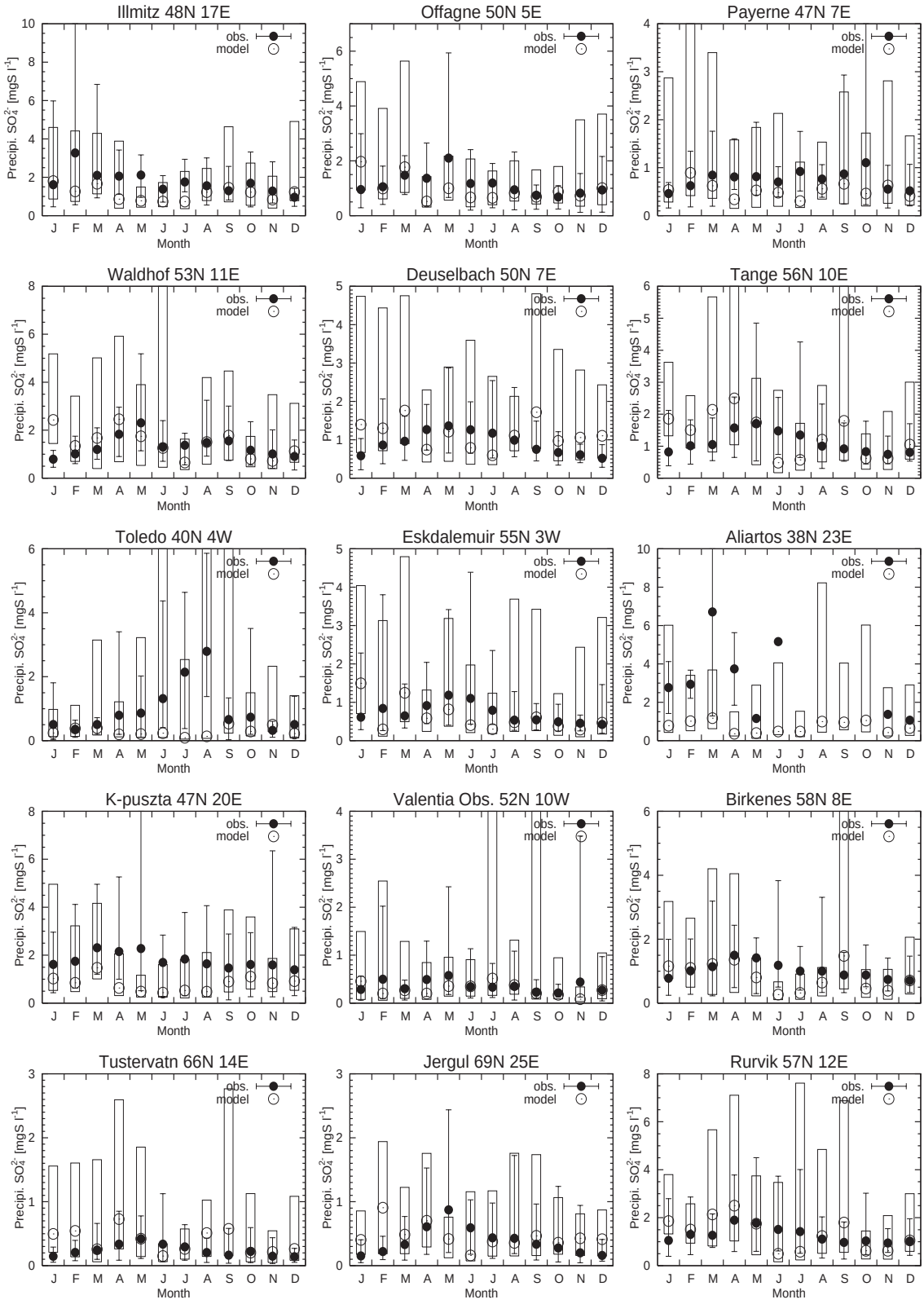

Figure 2.11. Same as Figure 2.10 but for SO_4^{2-} in precipitation (mgS l^{-1}).

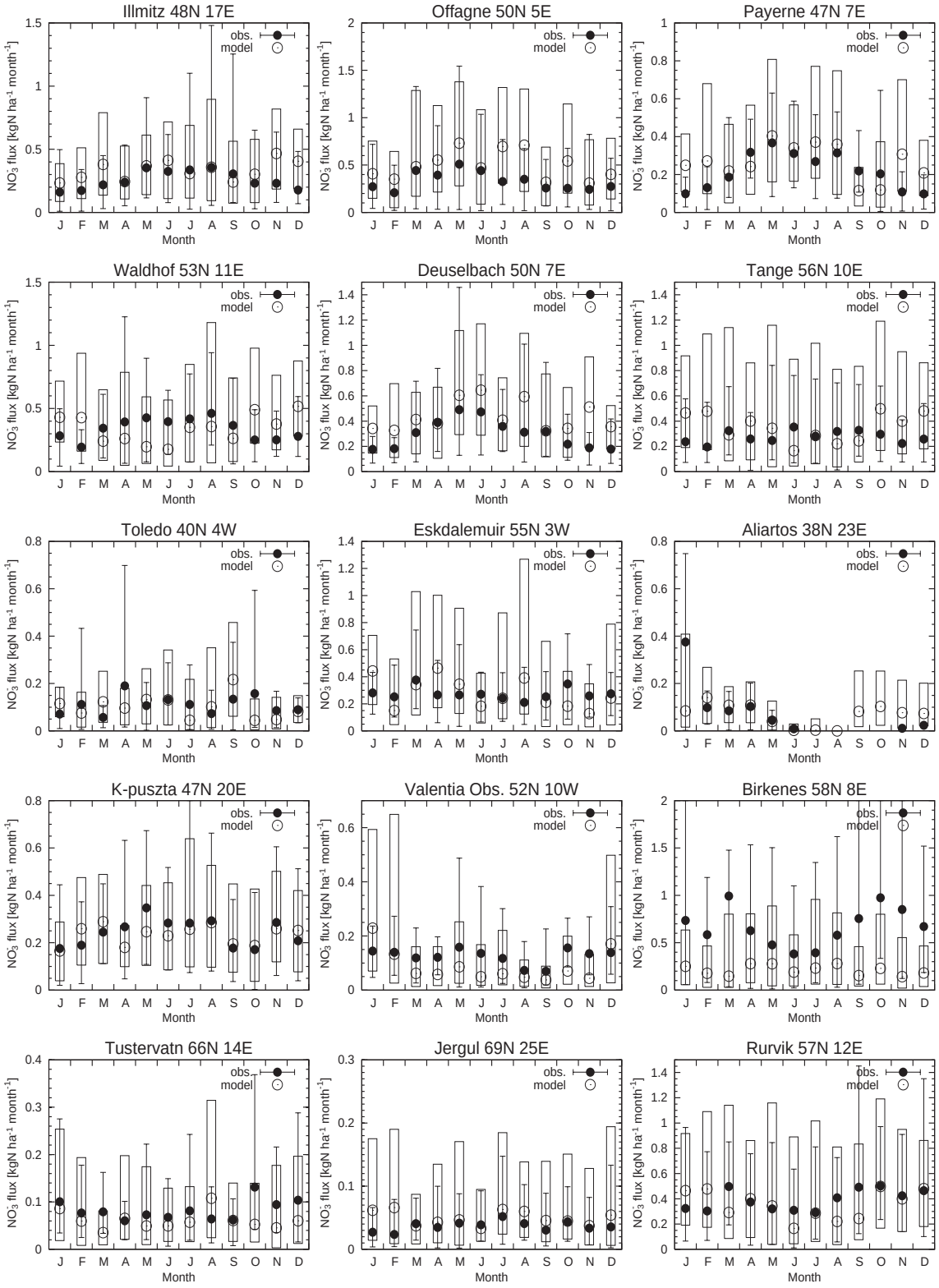

Figure 2.12. Seasonal variations of NO_3^- wet deposition flux (kgN ha^{-1} month^{-1}) observed (solid circles) and calculated (open circles with boxes showing the range) at the surface sites. The ranges of annual variation of the observation (during 1978-1995) are also shown with error bars. The observations are taken from the EMEP network.

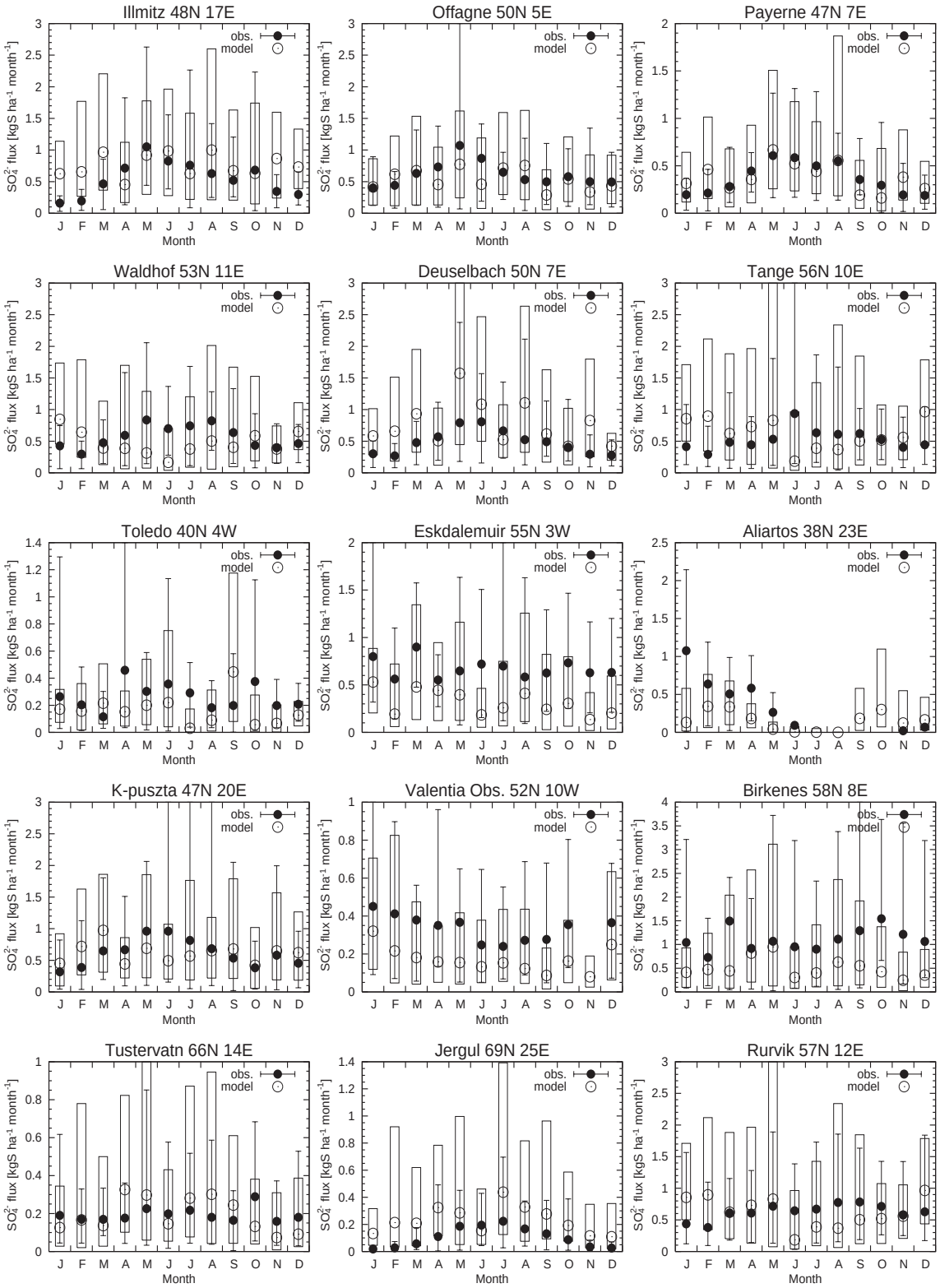

Figure 2.13. Same as Figure 2.12 but for SO_4^{2-} wet deposition flux (kgS ha^{-1} month^{-1}).